Thermally and Photoinduced Spin-Crossover Behavior in Iron(II)–Silver(I) Cyanido-Bridged Coordination Polymers Bearing Acetylpyridine Ligands

Carlos Cruz, Jorge Galdames, Liz Camayo-Gutierrez, Mathieu Rouzières, Corine Mathonière, Nieves Menendez, Nathalie Audebrand, Sebastian E Reyes-Lillo, Rodolphe Clérac, Diego Venegas-Yazigi, et al.

Thermally and Photoinduced Spin-Crossover Behavior in Iron(II)−Silver(I) Cyanido-Bridged Coordination Polymers Bearing Acetylpyridine Ligands

Carlos Cruz,* Jorge Galdames, Liz Camayo-Gutierrez, Mathieu Rouzières, Corine Mathonière, Nieves Menéndez, Nathalie Audebrand, Sebastian E. Reyes-Lillo, Rodolphe Clérac,* Diego Venegas-Yazigi, and Verónica Paredes-García*

We report two new cyanido-bridged Fe(II)−Ag(I) coordination polymers using different acetylpyridine isomers, $\{Fe(4acpy)_2[Ag(CN)_2]_2\}$ **1** and $\{Fe(3acpy)[Ag(CN)_2]_2\}$ **2** (4acpy = 4-acetylpyridine; 3acpy = 3-acetylpyridine) displaying thermally and photoinduced spin crossover (SCO). In both cases, the acetylpyridine ligand directs the coordination polymer structure and the SCO of the materials. Using 4-acetylpyridine, a two-dimensional (2D) structure is observed in **1** made of layers stacked on each other by silver−ketone interactions leading to a complete SCO and reversible thermally and photoswitching of the magnetic and optical properties. Changing the acetyl group to a 3-position, a completely different structure is obtained for **2**. The unexpected coordination of the carbonyl group to the Fe(II) centers induces a three-dimensional (3D) structure, leading to statistical disorder around the Fe(II) with three different coordination spheres, $[N_6]$, $[N_4O_2]$, and $[N_5O]$. This disorder gives rise to an incomplete thermally induced SCO with a poor photoswitchability. These results demonstrate that the choice of the acetyl position on the pyridine dictates the structural characteristics of the compounds with a direct impact on the SCO behavior. Remarkably, this work opens interesting perspectives for the future design of Fe−Ag cyanido coordination polymers with judiciously substituted pyridine ligands to tune the thermally and photoinduced SCO properties.

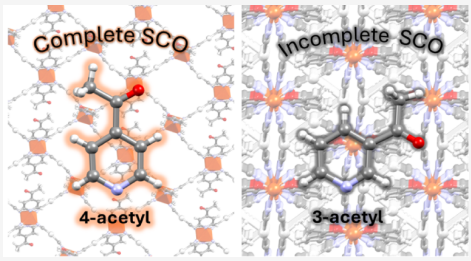

Transition metal ions display different electronic configurations depending on their geometries and oxidation states. For example, first-row transition metals with $3d^4$−$3d^7$ electronic configurations under an octahedral crystal field can exhibit two electronic states with different spin multiplicities: high spin (HS) and low spin (LS) states. Interestingly, when the crystal field energy is close to the pairing energy, the metal cation undergoes a crossover from one spin state to the other induced by an external stimulus such as temperature, light, or pressure.[1] The complexes containing such metal cations form so-called spin crossover (SCO) compounds. Some of these SCO materials are among the most prominent candidates for molecular switching devices due to their spin changes occurring near room temperature (RT).[2,3] The SCO phenomenon has a molecular origin, but the substantial alteration of volume at the metal ion can have a major impact on the whole material, for example, in the presence of an extended network of supramolecular elastic interactions (such as host−guest, hydrogen bonding, π−π interactions), commonly referred to as cooperativity. These interactions facilitate tivity reaches a significant strength, SCO may be accompanied by a first-order phase transition (also known as a spin transition), which is often associated with thermal hysteresis. Nevertheless, ensuring effective tuning over SCO properties continues to pose a challenge, largely due to the uncertainties inherent in crystal engineering and the control of these supramolecular interactions.[4] Another strategy to obtain a cooperative SCO or spin transition is to use ligands to bridge SCO metal ions into one-dimensional (1D), two-dimensional (2D), or three-dimensional (3D) coordination polymers (CPs).[5,6] In this context, a special type of CPs called Hofmann networks[7] exhibits remarkable SCO properties with wide thermal hysteresis close to RT.[8] In these CPs, an Fe(II) center is coordinated to four *N*-atoms coming from cyanidometallates such as $[M(CN)_4]^{2-}$ (M = Ni(II), Pd(II), and Pt(II)) or $[M(CN)_2]^-$ (M = Cu(I), Ag(I), and Au(I)). The Fe(II)

hexacoordination is reached with two *N*-donor organic ligands, commonly pyridine or pyrazine derivatives. Although the overall structure backbone of these CPs is well-known, SCO properties are strongly affected by the nature of the heterocyclic ligands.[9,10] Using linear ditopic ligands such as pyrazine, 3D structures are obtained with strong cooperativity, showing thermo-, photo-, and chemo-switching properties.[11] Additionally, functional groups on the heterocyclic organic ligands can be used as active sites for host−guest interactions.[12] When the axial ligand is a monodentate *N*-donor heterocycle (*e.g.*, pyridine), a 2D structure is stabilized. In this case, the weak interlayer interactions can trigger flexible crystalline packing, which can be the starting point for tuning the SCO properties. Additionally, the nature of the cyanidometallate moiety affects the structural and SCO properties of the Hofmann CPs. Due to their linear geometry, the $[M(CN)_2]^-$ units have been proposed as versatile building blocks to obtain SCO materials with interpenetrated structures and supramolecular metallophilic interactions. When pyridine (py) and $[Ag(CN)_2]_2^-$ are used,[8] the $\{Fe(py)_2[Ag(CN)_2]_2\}$ compound possesses a square grid coordination network, $\{Fe[Ag(CN)_2]_2\}$, decorated by two pyridines in the axial positions of the octahedral Fe(II) center.[13] The stacking of the layer is ensured by weak supramolecular interactions between the pyridine rings.[13] This compound shows a two-step incomplete SCO at rather low temperatures (98 and 146 K for the heating mode). The $\{Fe(n\text{R-py})_2[Ag(CN)_2]_2\}$ family of Hofmann CPs, in which *n*R-py is a substituted pyridine acting as capping ligand (n = 2, 3, 4 is the position of the R substituent in the pyridine ring), shows a 2D structure in most of the cases. Using the bulky ligand 4-styrylpyridine, Wang *et al.* reported SCO at a higher temperature (212 K) due to stronger layer contacts between the styryl substituents.[14] Additionally, pyridine with alkyl, halogen,[15−17] cyano, and *O*-functional substituents[18,19] promotes the Ag(I)···Ag(I) interactions in this family of compounds. Other supramolecular interactions involving Ag(I) and Fe(II) can be used to obtain stepwise SCO and host-dependent properties.[20−22] Curiously, these supramolecular interactions have been somewhat scarcely studied in Fe(II)−Ag(I) cyanido complexes. This structural characteristic offers an interesting opportunity to modulate the SCO properties of these $\{Fe(n\text{R-py})_2[Ag(CN)_2]_2\}$ Hofmann CPs by playing on the interlayer interactions with different substituted pyridine ligands while trying to maintain the 2D $\{Fe[Ag(CN)_2]_2\}$ structure. Following this idea, two new Fe(II)−Ag(I) cyanido-based materials using acetylpyridine as ligand are reported, $\{Fe(4acpy)_2[Ag(CN)_2]_2\}$ **1** and $\{Fe(3acpy)[Ag(CN)_2]_2\}$ **2** (4acpy = 4-acetylpyridine and 3acpy = 3-acetylpyridine). In both cases, this work demonstrates the key role of the acetyl substituent position in dictating the resulting crystal structure and the associated SCO properties. These results illustrate how careful functionalization of the *N*-donor ligand in Fe(II)/$[M(CN)_2]^-$ materials could offer new opportunities to design tunable SCO coordination polymers.

The solvents and reagents used for the synthesis were purchased from Sigma-Aldrich and Merck and used without any further purification. Synthesis of **1** and **2** was performed by direct mixing of the starting materials or using diffusion techniques. The same products were obtained in all cases regardless of the ratio used between Fe:Ag:*n*-acpy (see Supporting Information).

Synthesis of $\{Fe(4acpy)_2[Ag(CN)_2]_2\}$ 1 and $\{Fe(3acpy)[Ag(CN)_2]_2\}$ 2. Compounds **1** and **2** were synthesized as polycrystalline orange powders by the direct mixing of a 1:1 water−ethanol solution of $Fe(ClO_4)_2{\cdot}xH_2O$ and *n*-acetylpyridine (n = 4 for **1** and n = 3 for **2**) with $K[Ag(CN)_2]$ in water. Dark orange single crystals of **1** and **2** suitable for single-crystal X-ray diffraction were obtained using different slow diffusion techniques detailed in Supporting Information. Percentage calculated from the empirical formula $C_{18}H_{14}N_6O_2FeAg_2$ for **1** (in %): C, 34.98; H, 2.29; N, 13.60. Elemental Analysis (in %): C, 35.80; H, 2.50; N, 13.71. Percentage calculated from the empirical formula $C_{11}H_7N_5OFeAg_2$ for **2** (in %): C, 26.59; H, 1.42; N, 14.10. Elemental Analysis (in %): C, 26.54; H, 1.71; N, 13.41.

X-ray Data Collection and Structure Determination. Single crystals were directly picked up from the reaction media as described in Supporting Information, immediately immersed in a drop of Paratone oil, and mounted with a cryo-loop on a four-circle D8 VENTURE Bruker AXS (**1** at 270 and 150 K and **2** at 150 K) or APEXII Bruker diffractometer (**2** at 296 K) using Mo Kα radiation (λ = 0.71073 Å). Frame integration and data reduction were carried out with SAINT,[23] and the SADABS program was employed for multiscan-type absorption corrections.[24] Using the Olex2 package,[25] the crystal structures were solved with the ShelXT[26] structure solution program using dual methods and refined with the ShelXL package[27] using least-squares minimization based on F^2. The structures were refined using $P2_1/n$ and $C2/c$ space groups for **1** and **2**, respectively. Crystallographic details on data collection and refinement parameters of the crystal structures are summarized in Tables 1 and 2. The low-

Table 1. Crystal Data for 1[a]

sample	**1**-150 K	**1**-270 K
empirical formula	$C_{18}H_{14}Ag_2FeN_6O_2$	$C_{18}H_{14}Ag_2FeN_6O_2$
diffractometer	D8 VENTURE	D8 VENTURE
formula weight	617.94	617.94
temperature/K	150	270
crystal system	monoclinic	monoclinic
space group	$P2_1/n$	$P2_1/n$
a /Å	7.5830(6)	7.54500(10)
b /Å	13.6209(11)	14.1403(2)
c /Å	10.4943(9)	10.9150(2)
β /°	110.131(3)	110.480(7)
volume/Å^3	1017.71(15)	1090.90(5)
Z	2	2
ρ_{calc} /g cm^{-3}	2.017	1.881
μ/mm^{-1}	2.635	2.458
crystal size/mm^3	0.12 × 0.07 × 0.05	0.12 × 0.07 × 0.05
radiation	Mo Kα (λ = 0.71073 Å)	Mo Kα (λ = 0.71073 Å)
2θ range for data collection/°	5.102−54.948	4.916−54.962
reflections collected	11 403	7687
independent reflections	2331 [R_{int} = 0.0304, R_{sigma} = 0.0248]	2464 [R_{int} = 0.0298, R_{sigma} = 0.0294]
data/restraints/parameters	2331/0/134	2464/0/134
goodness-of-fit on F^2	1.117	1.060
final R indexes [$I \geq 2\sigma(I)$]	R_1 = 0.0198, wR_2 = 0.0460	R_1 = 0.0282, wR_2 = 0.0622
final R indexes [all data]	R_1 = 0.0211, wR_2 = 0.0468	R_1 = 0.0368, wR_2 = 0.0660
largest diff. peak/hole/e Å^{-3}	1.16/−0.55	0.94/−0.67

[a]Conventional $R_1 = \Sigma||F_o| - |F_c||/\Sigma|F_o|$; $wR_2 = [\Sigma w(F_o^2 - F_c^2)^2/\Sigma w(F_o^2)^2]^{1/2}$; $S = [\Sigma w(F_o^2 - F_c^2)^2/(\text{no. data} - \text{no. params})]^{1/2}$ for all data.

Table 2. Crystal Data for 2[a]

sample	2-150 K	2-296 K
empirical formula	$C_{11}H_7Ag_2FeN_5O$	$C_{11}H_7Ag_2FeN_5O$
diffractometer	D8 VENTURE	APEX II
formula weight	496.81	496.81
temperature/K	150	296
crystal system	monoclinic	monoclinic
space group	*C*2/c	*C*2/c
a /Å	16.222(4)	15.7961(9)
b /Å	13.544(3)	13.5737(8)
c /Å	7.641(2)	7.6992(4)
β /°	119.745(9)	117.374(2)
volume /Å^3	1457.6(7)	1465.95(14)
Z	4	4
ρ_{calc} /g cm^{-3}	2.264	2.251
μ /mm^{-1}	3.642	3.622
crystal size/mm^3	0.18 × 0.15 × 0.1	0.058 × 0.052 × 0.03
radiation	Mo Kα (λ = 0.71073 Å)	Mo Kα (λ = 0.71073 Å)
2θ range for data collection /°	4.172−55.048	4.176−61.768
reflections collected	7523	14 232
independent reflections	1626 [R_{int} = 0.0467, R_{sigma} = 0.0362]	2233 [R_{int} = 0.0457, R_{sigma} = 0.0391]
data/restraints/parameters	1626/132/132	2233/129/122
goodness-of-fit on F^2	1.412	1.193
final R indexes [$I \geq 2\sigma(I)$]	R_1 = 0.0445, wR_2 = 0.1248	R_1 = 0.0406, wR_2 = 0.0654
final *R* indexes [all data]	R_1 = 0.0513, wR_2 = 0.1459	R_1 = 0.0686, wR_2 = 0.0701
largest diff. peak/hole/e Å^{-3}	0.94/-1.19	0.85/-0.80

[a]Conventional $R_1 = \Sigma||F_0| - |F_c||/\Sigma|F_0|$; $wR_2 = [\Sigma w(F_0^2 - F_c^2)^2/\Sigma w(F_0^2)^2]^{1/2}$; $S = [\Sigma w(F_0^2 - F_c^2)^2/(\text{no. data} - \text{no. params})]^{1/2}$ for all data.

temperature data of **2** were also refined using the noncentrosymmetric *Cc* space group with close reliability factors. Nevertheless, considering the Mössbauer results, the *C*2/*c* space group better describes the structure of **2** at both temperatures (296 and 150 K). Structure drawings have been made with Mercury and TOPOS software.[28] Additional information concerning the crystal and refinement parameters is detailed in Supporting Information.

The X-ray powder diffraction data were collected at RT on a PANalytical X'Pert MPD diffractometer with Cu K$\alpha_{1,2}$ radiation equipped with an X'celerator detector in the range of 4°< 2θ < 80°. Indexing of the powder patterns was done with the program DICVOL14 through the PreDICT interface.[29] The whole powder pattern fittings (with the Le Bail approach) were done employing the FULLPROF program[30] available in the software package WinPLOTR.[31] The experimental powder X-ray diffraction patterns of the compounds agree with the theoretical patterns generated from the crystal structures. This result confirms that the synthesized polycrystalline samples and the obtained single crystals are the same crystalline materials (Figure S1a,b).

Thermogravimetric Analysis. Thermogravimetric analyses were performed on a Mettler Toledo TGA/DSC-II system. The samples were introduced into an alumina holder and heated under air from RT to 900 °C with a heating rate of 5 °C/min (Figure S2).

Spectroscopic and Optical Measurements. *2.4.1. Infrared Spectroscopy.* Infrared spectra of **1** and **2** and the organic ligands, 4-acetylpyridine and 3-acetylpyridine, were recorded on an attenuated total reflectance Fourier transform infrared, ATR-FTIR-4000 Jasco spectrometer, in the 4000−400 cm^{-1} range without using any support (Figure S3).

Energy-Dispersive X-ray Spectroscopy. The estimation of the Fe and Ag wt % for bulk samples of **1** and **2** was done by energy-dispersive spectroscopy (EDXS) for Fe-26 K-series and Ag-47 L-series using a Bruker Tescan Vega3 LMH (LaB_6) scanning electron microscope coupled with an energy-dispersive detector (Figure S4).

Mössbauer Spectroscopy. Mössbauer spectra were recorded for **1** and **2** using a conventional constant acceleration spectrometer equipped with a ^{57}Co (Rh) source. A flow cryostat RICOR MCH 5B was used to obtain the spectra between 77 and 300 K. To avoid saturation effects, the thickness of the sample was 10 mg of natural Fe cm^{-2}. The spectra were fitted by doublets of Lorentzian lines using the NORMOS program.[33] Isomer shift data were referred to metallic iron at RT (also used for velocity calibration).

Optical Reflectivity. The surface optical reflectivity measurements have been performed with a home-built system, operating between 10 and 300 K and in a 400−1000 nm spectrometric range. A halogen-tungsten light source (Leica CLS 150 XD tungsten halogen source adjustable from 0.05 to 1 W cm^{-2}) was used as the spectroscopic light. The measurements were calibrated by a NIST traceable standard for reflectance (sphereOptics, ref SG3054). As the samples are potentially very photosensitive, the light exposure time was minimized during the experiments, keeping the samples in the dark except during the spectra measurements when white light is shined on the sample surface (p = 0.08 mW cm^{-2}). For all the excitation/de-excitation experiments performed at 10 K, the sample was initially placed at this temperature keeping the sample in the dark to avoid any excitation. Heating and cooling measurements were carried out at 4 K min^{-1}. The source described above was used for white light irradiation but in a continuous manner with a power of 0.08 mW cm^{-2}. Light-emitting diodes (LEDs) operating between 365 and 1050 nm (from Thorlabs) were used for other excitation experiments.

Magnetic and Photomagnetic Measurements. Magnetic susceptibility measurements were recorded with a Quantum Design MPMS-XL SQUID magnetometer, operating with applied fields up to 7 T at temperatures from 1.85 to 400 K. The data were collected on 14.14 mg of **1** and 16.45 mg of **2**, placed in a polypropylene bag (17.76 and 16.78 mg, respectively), and inserted in a plastic straw. Prior to the experiments, the field-dependent magnetization was measured at 100 K to detect the presence of any bulk ferromagnetic impurities. The samples appeared to be free of any significant ferromagnetic impurities.

The photomagnetic experiments were performed using a set of light-emitting diodes (LEDs from Thorlabs) operating between 365 and 1050 nm, coupled *via* an optical fiber to the cavity of a Quantum Design MPMS-XL magnetometer. 0.37 mg of **1** and 0.26 mg of **2** were maintained in 3.63 and 3.36 mg polypropylene bags, respectively, and inserted in a plastic straw. Note that the temperatures have been corrected to consider the light irradiation heating (an average of +2 K has been observed, for example, with red light). Experimental susceptibilities were corrected for sample holder and intrinsic diamagnetic contributions.

Theoretical Studies. Periodic lattice spin-polarized density functional theory (DFT) calculations were performed using the Vienna Ab initio Simulation Package (VASP).[34,35] The generalized gradient approximation of Perdew, Burke, Ernzerhof revised for solids (PBEsol)[36] plus the Hubbard U method[37] were used to describe the Fe *d*-orbitals. The DFT + U method has been shown to correct the delocalization error of semilocal functionals such as PBEsol and improve the description of *d*-orbitals at a low computational cost. Several values of *U* are proposed in the literature for the case of an Fe site in an O environment;[38−40] however, to the best of our knowledge, there is no available value of *U* for an Fe site with N or a mixture of O and N environment. In this work, total energies and structural parameters are obtained for Hubbard *U* values ranging from 0 to 6 highlighting the typical values of U_{Fe} within an O environment. Our calculations for **1** and **2**, containing 4 and 2 Fe sites, respectively, used a plane-wave energy cutoff of 500 eV, 4 × 2 × 2 Monkhorst−Pack *k*-point grids, and projected augmented pseudopotentials with 17, 14, 6, 5, 4, and 1 valence electrons for Ag, Fe, O, N, C, and H, respectively, from the VASP library.[41] Structural relaxations were performed using the PBEsol + U functional until atomic forces were smaller than 0.01

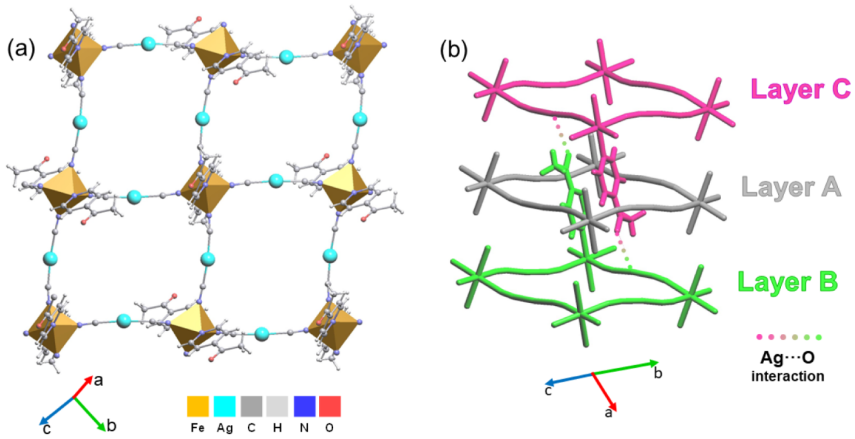

Figure 1. Views of the crystal structure of **1** at 270 K: (a) showing an $\{Fe[Ag(CN)_2]_2\}$ layer exhibiting a quasi-square 2D structure; (b) showing the packing of the three successive layers (A, B, and C) interacting *via* Ag···O interactions to form a triple interlocked supramolecular structure.

eV/Å. Octahedral distortions are obtained with the software SHAPE.[42]

Synthesis and Structural Analysis. $\{Fe(4acpy)_2[Ag(CN)_2]_2\}$ **1** and $\{Fe(3acpy)[Ag(CN)_2]_2\}$ **2** were obtained using 4-acetylpyridine (4acpy) and 3-acetylpyridine (3acpy), respectively (see Supporting Information and experimental part). It is worth mentioning that attempts to obtain an analogous compound with 2-acetylpyridine were unsuccessful. The single-crystal structure of **1** was solved at 270 K (HT = high temperature) and 150 K (LT = low temperature; Table 1) in the same monoclinic $P2_1/n$ space group. At both temperatures, the asymmetric unit is the same and involves a unique Fe center, two 4acpy ligands, and two dicyanidoargentate anions. Symmetry elements lead to the expected 2D $\{Fe[Ag(CN)_2]_2\}$ CP (Figure 1a). The unique Fe(II) site shows an $[N_6]$ octahedron formed by four CN^- atoms belonging to four $[Ag(CN)_2]^-$ units and two pyridine rings belonging to 4-acetylpyridine ligands (Figure S5a). At 270 K, the Fe−N distances above 2.12 Å support the presence of Fe(II) centers in their high-spin $S = 2$ state: Fe1−$N2_{cyanido}$ = 2.126(2) Å, Fe1−$N3_{cyanido}$ = 2.147(2) Å, and Fe1−$N1_{py}$ = 2.223(2) Å (Table 3).

Table 3. Principal Bond Lengths of 1 and 2

		bond length in Å			
		1-150 K	**1**-270 K	**2**-150 K	**2**-296 K
Fe1	$N1_{py}$	2.0076(15)	2.223(2)	2.090(6)	2.118(3)
Fe1	$N2_{cyanido}$	1.9395(15)	2.126(2)	2.094(6)	2.126(3)
Fe1	$N3_{cyanido}$	1.9480(15)	2.147(2)	2.26(3)	2.25(3)
Fe1	$O1_{acetyl}$			2.14(2)	2.179(19)

On the other hand, the unique Ag(I) site has a quasi-linear $[C_2]$ coordination environment with Ag1−C8 = 2.053(3) Å and Ag1−C9 = 2.057(3) Å and a C8−Ag1−C9 angle of 173.17(12)°. Furthermore, the $[FeN_6]$ octahedra are connected by μ−$\kappa N,\kappa N'$-$[Ag(CN)_2]^-$ bridges forming an extended square grid with Fe(II) centers as nodes and $[Ag(CN)_2]^-$ as ditopic spacers with 4acpy playing the role of a capping ligand (Figures 1a and S5b). In the quasi-square $Fe_4[Ag(CN)_2]_4$ motif, the Fe···Fe distance is 10.4120(3) Å with Fe−Fe−Fe angles of 85.537(3)° and 94.463(3)° and Fe−N−C angles that deviate significantly from linearity: Fe1−N2−C8 = 173.9(3)° and Fe1−N3−C9 = 164.1(3)°. These geometric characteristics induce the corrugated topology of the $\{Fe[Ag(CN)_2]_2\}$ layer with the 4acpy ligand passing through the neighboring layers as shown in Figures 1b and S5b. Indeed, the pseudosquare $Fe_4[Ag(CN)_2]_4$ cavities are crossed by two 4acpy ligands belonging to the upper and lower layers as reported in the $\{Fe(py)_2[Ag(CN)_2]_2\}$ analog (Figure 1b). Nevertheless, the acetyl groups in **1** prevent $\pi\cdots\pi$ interactions of the pyridine rings but induce Ag(I)···ketone supramolecular interactions. For a given layer, the Ag(I) cations of the upper and lower layers interact with the C═O groups of the 4acpy ligand from the lower and upper layers, respectively (with an Ag···O distance of 3.051(3) Å). As shown in Figures 1b and S5c, these supramolecular contacts lead to a triple interlocked structure. As mentioned before, the space group of **1** is maintained at LT, but a substantial change in the crystallographic parameters can be observed. The unit cell volume decreases from 1090.90(5) $Å^3$ at HT to 1017.71(15) $Å^3$ at LT corresponding to a net compression of 6.7%. Looking closely at the bond distances, an important shortening of Fe−N bonds (~0.2 Å, around 9%) is observed at LT (Table 3). The bond lengths reach Fe1−$N1_{py}$ = 2.0076(15) Å, Fe1−$N2_{cyanido}$ = 1.9395(15) Å, and Fe1−$N3_{cyanido}$ = 1.9480(15) Å, a decrease of around 0.15−0.2 Å in the overall Fe−N bonds (6.6, 8.8, and 9.3%, respectively), in agreement with an Fe center in its low-spin $S = 0$ state. This change in the Fe−N distances also impacts the regularity of the octahedral coordination sphere. The distortion parameters computed with OctaDist[43] are Σ = 9.17°, Θ = 31.52° for $[FeN_6]$ at HT and Σ = 5.66°, Θ = 20.93° for $[FeN_6]$ at LT. This geometrical change shows that the $[FeN_6]$ octahedra present *cis* N−Fe−N angles closer to 90° and less trigonal distortion at LT due to more similar Fe−N bond distances. A continuous shape measure (CShM) can also be done using SHAPE[42] for the $[FeN_6]$ octahedra. These calculations gave a CShM of 0.05042 and 0.02782 for $[FeN_6]$ at 270 and 150 K, respectively (Table S1), which confirms that the $[FeN_6]$ octahedron becomes more regular at LT as expected in the presence of an SCO process.[44] This thermal SCO and the associated modification of the Fe coordination sphere also induce a decrease in both $\{Fe[Ag(CN)_2]_2\}$ grid dimensions

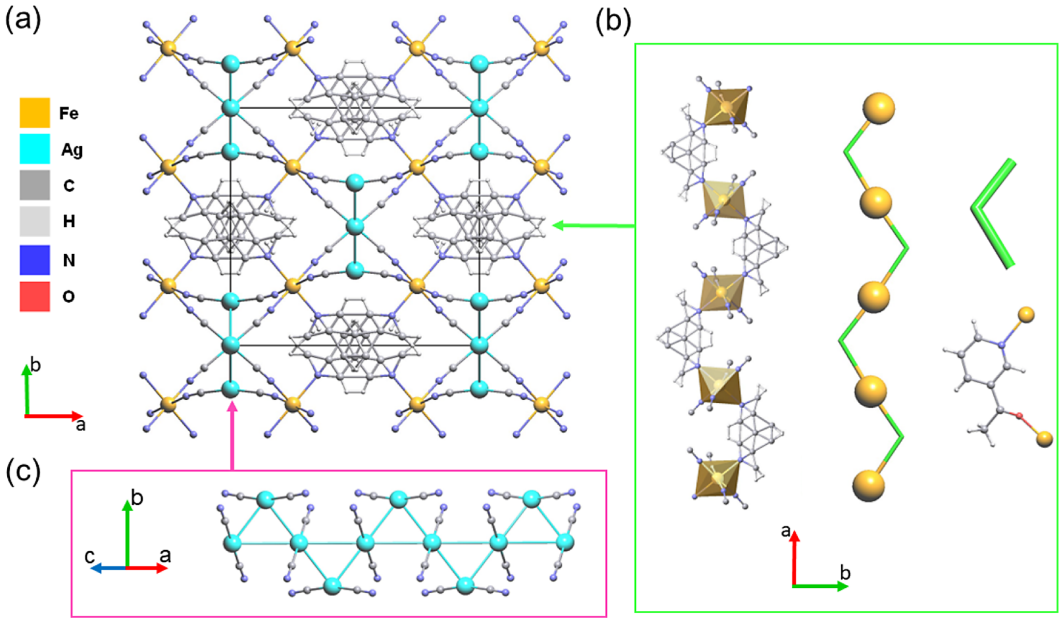

Figure 2. Views of the crystal structure of **2** at 296 K: (a) along the *c* direction; (b) showing the $[Fe(3acpy)]^{2+}$ zigzag chain running along the *a** axis and the bidentate coordination mode of the 3acpy ligand; (c) showing the $[Ag(CN)_2]_2^{2-}$ chains formed by argentophilic interactions.

and Fe···Fe distances from 10.4120(3) Å at 270 K to 10.0987(5) Å at 150 K.

As shown above, the use of the 4-acetylpyridine ligand leads to a 2D SCO coordination polymer reminiscent of the $\{Fe(py)_2[Ag(CN)_2]_2\}$ analog but with new Ag−ketone interactions, which stabilize a triple-interlocked supramolecular structure.

To further explore the effect of ligand functionalization on the magnetostructural properties of this family of SCO materials, the 3-acetylpyridine ligand was used to synthesize compound **2**. The crystal structure of **2** was solved at 296 and 150 K (Table 2; HT and LT, respectively) in the *C*2/*c* space group with an asymmetric unit composed of a unique Fe(II) center, two dicyanidoargentate fragments, and a disordered 3acpy ligand. The LT data of **2** can also be refined using the noncentrosymmetric *Cc* space group. Using this alternative space group, the 3acpy disorder is resolved with reliability factors similar to those of the *C*2/*c* space group. However, considering the results below, the *C*2/*c* space group was preferred for the HT and LT data.

Unexpectedly, the structures of **1** and **2** are completely different (Figure 2a). In **2**, the disordered 3acpy ligand coordinates to the Fe(II) center in its axial positions by both pyridine and ketone groups forming a $[Fe(3acpy)]^{2+}$ zigzag chain along the *a**-direction (Figures 2b and S6a). Furthermore, the two linear $[Ag(CN)_2]^-$ fragments arrange through extended Ag···Ag interactions forming a $[Ag(CN)_2]_2^{2-}$ chain along the [101] direction (Figure 2c). The Ag1 and Ag2 ions show argentophilic Ag_4 and Ag_2 arrangements, respectively, forming isosceles Ag_3-triangles along the chain (Figures 2c and 3a). The cyanido groups of the $[Ag(CN)_2]_2^{2-}$ chains coordinate to the Fe(II) center in its four equatorial positions (at HT: $Fe1{-}N1_{cyanido}$ = 2.118(3) Å and $Fe1{-}N2_{cyanido}$ = 2.126(3) Å; Figure S6b) to stabilize a three-dimensional coordination polymer. The 3acpy ligand lies on a 2-fold axis that passes through the C6 atom (red line in Figure 3b), the carbon atom that connects the pyridine ring with the ketone group. Consequently, the disorder of the 3acpy ligand induces a complex situation with a quasi-superposition of the $N3_{pyridine}$ and $O1_{ketone}$ atoms, and the $C4_{pyridine}$ and $C9_{methyl}$ atoms with 50% occupancies. The partial occupancy of the coordinated $N3_{pyridine}/O1_{ketone}$ atoms induces three possible coordination spheres for the Fe site: $[FeN_6]$, $[FeN_4O_2]$, and $[FeN_5O]$ (Figures 3c and S6b,c), with $Fe1{-}N3_{pyridine}$ = 2.25(3) Å and $Fe1{-}O1_{ketone}$ = 2.179(19) Å. In the case of a stochastic disorder, the probability of finding these chemical environments around the Fe center is 25, 50, and 25%, respectively.

Upon lowering the temperature, a negligible compression of the unit cell of **2** is observed as exemplified by the small decrease (less than 1%) of the unit cell volume from 1465.95(14) $Å^3$ at HT to 1457.6(7) $Å^3$ at LT. Due to the 3acpy disorder and the presence of different Fe coordination spheres, a comparison of the average Fe−N and Fe−O bond lengths is not as straightforward as for **1**. Globally, a small decrease in the bond lengths is observed. The equatorial $Fe{-}N_{cyanido}$ bonds decrease to $Fe1{-}N1_{cyanido}$ = 2.090(6) Å and $Fe1{-}N2_{cyanido}$ = 2.094(6) Å at LT (less than 2%), while the $Fe1{-}N3_{pyridine}$ and $Fe1{-}O1_{ketone}$ bonds stay roughly the same (HT/LT: 2.25(3)/2.26(3)and 2.179(19)/2.14(2) Å, respectively). As the 3acpy disorder induces an average crystal structure, it is impossible to use these structural data to discuss a possible SCO phenomenon for one or more of the three different Fe centers.

Mössbauer Spectroscopy. The above analysis of the crystal structure of **1** concludes with the presence of an SCO process at the Fe(II) site. Mössbauer spectroscopy performed as a function of temperature further supports this conclusion. At 290 K, the spectra shown in Figure S7 are composed of a single doublet possessing the characteristic hyperfine parameters (isomer shift and quadrupole splitting, ΔE_Q) of a high-spin Fe(II) center surrounded by six nitrogen atoms (Table 4). As the temperature decreases, a second doublet appears with δ and ΔE_Q values that can be assigned to a low-spin Fe(II)

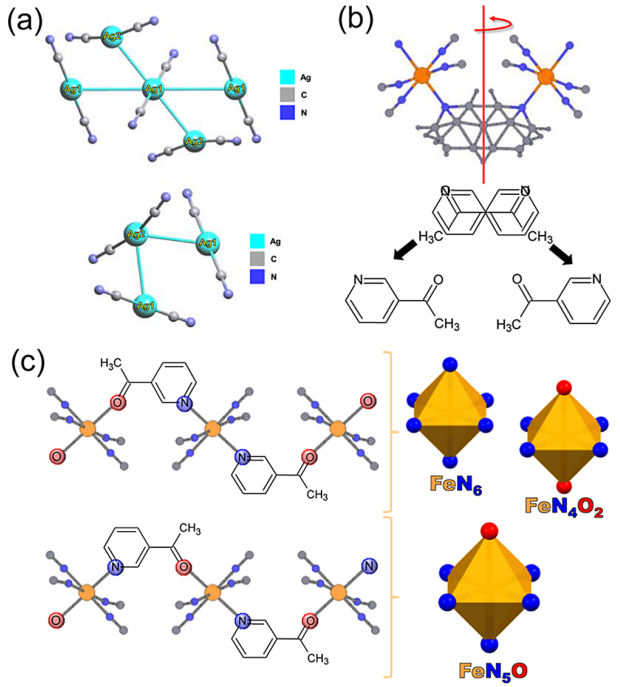

Figure 3. Additional views of the crystal structure of **2** at 296 K: (a) Ag···Ag interactions connecting the $[Ag(CN)_2]^-$ fragments into chains. The Ag1 and Ag2 metal ions have an AgC_2 environment with linear and pseudolinear geometry (C1−Ag1−C1#a = 180° and C2−Ag2−C2#b = 168.22°; #a = $-x$, 1 − y, $-z$; #b = 1 − x, y, 1/2 − z). In Ag···Ag interactions, Ag1 and Ag2 have Ag_2 linear (Ag2#c−Ag1−Ag2#d = 180°; #c: $-1/2 + x$, $1/2 + y$, z; #d: $1/2 - x$, $1/2 - y$, $-z$) and Ag_2 bent (Ag1#e−Ag2−Ag1#f = 77.55°; #e: $1/2 + x$,$-1/2 + y$,z; #f: $1/2 - x$,$-1/2 + y$,$1/2-z$) arrangements, respectively (Ag1···Ag2#c = 3.1540(4) Å). The Ag1 ions also show a direct but weaker Ag1···Ag1#g interaction (#g= $-x$,y,$1/2 - z$; Ag1···Ag1#g = 3.850 Å); (b) showing the Fe-3acpy-Fe motif with the 3acpy ligand, which is disordered due to the 2-fold axis (red line) at the C6 carbon atom. A scheme of ligand disorder is also shown; (c) showing the three possible chemical environments, $[FeN_6]$, $[FeN_5O]$, and $[FeN_4O_2]$ induced by the ligand disorder.

Table 4. Mössbauer Hyperfine Parameters for 1

temperature	δ/mm s^{-1}	ΔE_Q/mm s^{-1}	area/%	
290 K	1.071(1)	0.745(1)	95(1)	$[FeN_6]$/HS
210 K	1.115(1)	1.097(3)	50(2)	$[FeN_6]$/HS
	0.456(1)	0.333(3)	46(2)	$[FeN_6]$/LS
150 K	0.466(1)	0.300(3)	95(1)	$[FeN_6]$/LS
77 K	0.474(1)	0.294(2)	95(1)	$[FeN_6]$/LS

center. This doublet is the only one remaining at 150 and 77 K (Figure S7), implying that a complete SCO is observed by Mössbauer spectroscopy in agreement with the structural analysis.

As expected, the analysis of the Mössbauer spectrum for **2** is not as straightforward as for **1**. Figure 4a−c shows the spectra of **2** at 290, 163, and 77 K. The spectrum at 290 K (Figure 4a) is composed of three well-defined doublets with hyperfine parameters characteristic of high-spin Fe(II) sites. As there is only one crystallographically independent Fe(II) center in **2**, the existence of three HS Fe(II) signals is simply the direct consequence of the 3acpy ligand disorder (*vide supra*) and the resulting coexistence of three different Fe chemical environments, $[FeN_6]$, $[FeN_5O]$, and $[FeN_4O_2]$ discussed in the structural section. Taking into account a point charge model for an octahedral resonant center, an increase in the electronegativity of the ligand will induce a lower density of *s*-electrons in the nucleus and thus an increase in the Fe(II) isomer shift (δ). Thus, δ should increase while adding O atoms in the Fe coordination sphere (Table 5 and Figure S8).

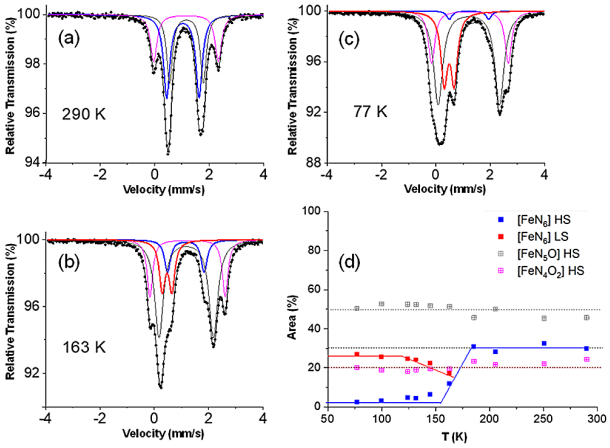

Figure 4. (a−c) ^{57}Fe Mössbauer spectra for **2** at 290, 163, and 77 K with the blue, red, gray, and pink solid lines corresponding to the fit of the high-spin $[FeN_6]$, low-spin $[FeN_6]$, high-spin $[FeN_5O]$, and high-spin $[FeN_4O_2]$ centers, respectively. See Table 5 for the fitting parameters. (d) Thermal evolution of the % area of Mössbauer doublets for the different chemical environments of the Fe site in **2**.

Table 5. Mössbauer Hyperfine Parameters for 2

temperature	δ/mm s^{-1}	ΔE_Q/mm s^{-1}	area/%	
290 K	1.076(1)	1.059(2)	30(3)	$[FeN_6]$/HS
	1.100(1)	1.324(2)	46(3)	$[FeN_5O]$/HS
	1.143(1)	2.382(2)	24(2)	$[FeN_4O_2]$/HS
163 K	1.162(1)	1.348(2)	12(2)	$[FeN_6]$/HS
	1.177(1)	2.000(2)	51(2)	$[FeN_5O]$/HS
	1.226(1)	2.762(2)	20(2)	$[FeN_4O_2]$/HS
	0.473(1)	0.356(2)	17(2)	$[FeN_6]$/LS
77 K	1.215(2)	1.45(1)	3(1)	$[FeN_6]$/HS
	1.210(1)	2.259(2)	50(1)	$[FeN_5O]$/HS
	1.252(1)	2.823(2)	20(1)	$[FeN_4O_2]$/HS
	0.488(1)	0.368(2)	27(1)	$[FeN_6]$/LS

Therefore, the doublet with the lower δ (1.076(1) mm s^{-1}) can be assigned to $[FeN_6]$ centers.[45,46] It is worth mentioning that this value of 1.076 mm s^{-1} is very similar to the one observed for the $[FeN_6]$ site in **1**. The other two doublets can then be easily assigned to $[FeN_5O]$ (1.100(1) mm s^{-1}) and $[FeN_4O_2]$ (1.143(1) mm s^{-1}), respectively.[47−49]

As the temperature decreases, an increase in δ and ΔE_Q for the three doublets is observed (Table 5 and Figure S8), most likely due to the second-order Doppler effect. A significantly greater variation of ΔE_Q for the $[FeN_5O]$ (C_{4v}) doublet is detected probably in relation to a lower distortion of the octahedral environment compared with $[FeN_6]$ and $[FeN_4O_2]$ centers (D_{4h}). Assuming that the Lamb−Mössbauer factor is the same in all positions of the lattice, the resonant area of each site can be related to the percentage of resonant atoms in each environment. Figure 4d shows around 25% contribution from $[FeN_6]$-HS and $[FeN_4O_2]$-HS respectively, while the remain-

ing 50% corresponds to $[FeN_5O]$. Around 170 K, a decrease in the signal intensity of $[FeN_6]$-HS is observed accompanied by the appearance of a fourth doublet. The parameters of the new low-temperature doublet are consistent with an Fe(II)-LS in an octahedral $[FeN_6]$ environment; thus, HS → LS crossover occurs at the $[FeN_6]$ centers below 170 K (Figure 4b). The SCO is complete around 100 K, leaving only 3% of residual $[FeN_6]$-HS (Figure 4c).[50]

The Mössbauer spectroscopy confirms the above crystal structure analysis of **2** and the presence of an unexpected *N,O*-bridging coordination of the 3acpy ligands leading to statistical disorder of the Fe(II) coordination sphere. The structural particularity induces an incomplete SCO of the Fe(II) site with the octahedral $[FeN_5O]$ and $[FeN_4O_2]$ sites (75% of the sites) remaining in their HS state down to low temperature, while the $[FeN_6]$ sites (25% of the sites) are experiencing an SCO.

First-Principles Calculations. Theoretical insight into the electronic structure of the Fe sites in these complexes has been obtained from periodic first-principles calculations (see Section 2 for details, Figures S9−S11 and Table S3).[51−55] For both structures **1** and **2**, LS and HS states were computed by constraining the total spin of the system to $S = 0$ and $S = 2$, respectively, and fully relaxing the internal coordinates and lattice parameters of the structures. Figure S9a shows the total energy and unit cell volume as a function of the Hubbard U parameter for **1**. As the on-site interaction U increases, the pairing energy increases, favoring the HS state over the LS state. For $U = 0$ (PBEsol), an LS configuration is predicted. However, for typical values of 3.71−5.30 eV for Fe sites with an O environment (highlighted area in gray; Figures S9 and S10),[38−40] there is a crossover between HS and LS, suggesting the possibility of an SCO, in agreement with our experimental results. It is important to note that DFT + U calculations are performed at zero temperature and therefore do not include an entropic contribution. The unit cell volume increases with U due to the depopulation of the bonding states and the concomitant bond increasing. We obtain 7.9 and 7.7% volume expansion between LS and HS states for $U = 4$ and 5 eV, respectively, in line with the experimental value of ∼7% (see Section 3.1). Additional theoretical results are shown in Figure S10a, which reports on the band gaps as well as octahedral distortions and octahedral volumes as a function of the Hubbard U parameter for **1**. The computed structure induces positive band gaps, leading to the expected insulating state. Moreover, the octahedral distortion values and volumes for large U values agree with those observed experimentally for the $[FeN_6]$ octahedron.

In the case of **2**, the symmetry of the unit cell, the local disorder, and different coordination sites for Fe centers are simulated considering two periodic systems. The first one (Model 1) considers four Fe sites in the unit cell coordinated to five nitrogen and one oxygen atom, $[FeN_5O]$, and the second (Model 2) considers two different Fe sites, two Fe centers coordinated to six nitrogen, $[FeN_6]$, and two Fe sites coordinated to four nitrogen and two oxygens, $[FeN_4O_2]$ (Figure S11). Figure S9b,c shows the total energy and unit cell volume as a function of the Hubbard U parameter for Model 1 and Model 2, respectively. For Model 1, the critical U parameter for SCO is slightly shifted to lower values. In addition, the measured volumes at LT (150 K) and HT (296 K) agree with the computed volume for the HS site. Altogether, and compared with the calculations obtained for **1**, these results are in line with the absence of SCO in **2** for $[FeN_5O]$ sites. Meanwhile, three possible spin configurations for Model 2 can be considered: HS with four Fe sites in high spin; LS with four Fe sites in low spin; MS, an intermediate case with an incomplete SCO in which two $[FeN_4O_2]$ sites remain in high spin and two $[FeN_6]$ sites are in low spin. In the frame of this model and for typical U values (highlighted area in gray; Figures S9 and S10), we observe an energetic competition among the HS, MS, and LS configurations, suggesting that the three proposed chemical environments are experimentally possible. Figure S10b,c shows the calculated band gaps as well as the octahedral distortions and octahedral volumes for Models 1 and 2. Similarly to **1**, these simulations display lower octahedral distortion values and octahedal volumes for the octahedra at LT in agreement with experimental results. This theoretical investigation supports that Fe(II) in $[FeN_5O]$ and $[FeN_4O_2]$ chemical environments stays in the HS state and induces at the bulk level an incomplete SCO driven by the $[FeN_6]$ sites.

Magnetic Properties. The DC magnetic properties of **1** and **2** have been investigated by measuring the thermal variation of their magnetic susceptibility (χ; Figure 5).

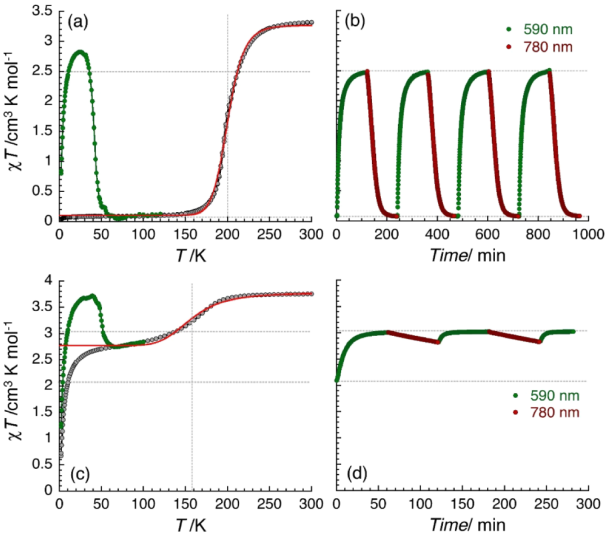

Figure 5. Magnetic and photomagnetic properties of **1** (a,b; top) and **2** (c,d; bottom). Parts (a, c): Temperature dependence of the χT product: in gray, at 1 T and 0.6 K/min in cooling and heating modes in the dark, and in green, at 1 T and 0.3 K/min in heating mode in the dark after being irradiated at 590 nm (1 mW cm^{-2}) during 4 and 2 h at 10 K for **1** and **2**, respectively. Parts (c,d): Time dependence of the χT product at 1 T and 10 K under successive irradiation at 590 nm (green; 1 mW cm^{-2}) and 780 nm (red; 1 mW cm^{-2}). Dotted gray lines are guides for the eyes for the $T_{1/2}$ and the χT amplitude of the photoswitchability; χ is the magnetic susceptibility calculated from the ratio of the magnetization, M, and the applied magnetic field, H, per mole of complex; solid red lines in parts (a,b) are the best fit to the ideal solution model (see main text).

Specifically for **1**, Figure 5a shows the χT product (at 1 T; gray dots) measured between 300 and 1.85 K (at 0.6 K/min) that is perfectly reproducible in heating and cooling modes highlighting the absence of significant thermal hysteresis or alteration of the material. At 300 K, the χT value is 3.3 cm^3 K mol^{-1} for **1**, which is close to the expected value for uncoupled Fe(II) spins in their high-spin $S = 2$ state (3 cm^3 K mol^{-1}, $g = 2$), suggesting a g value around 2.10. A smooth diminution of

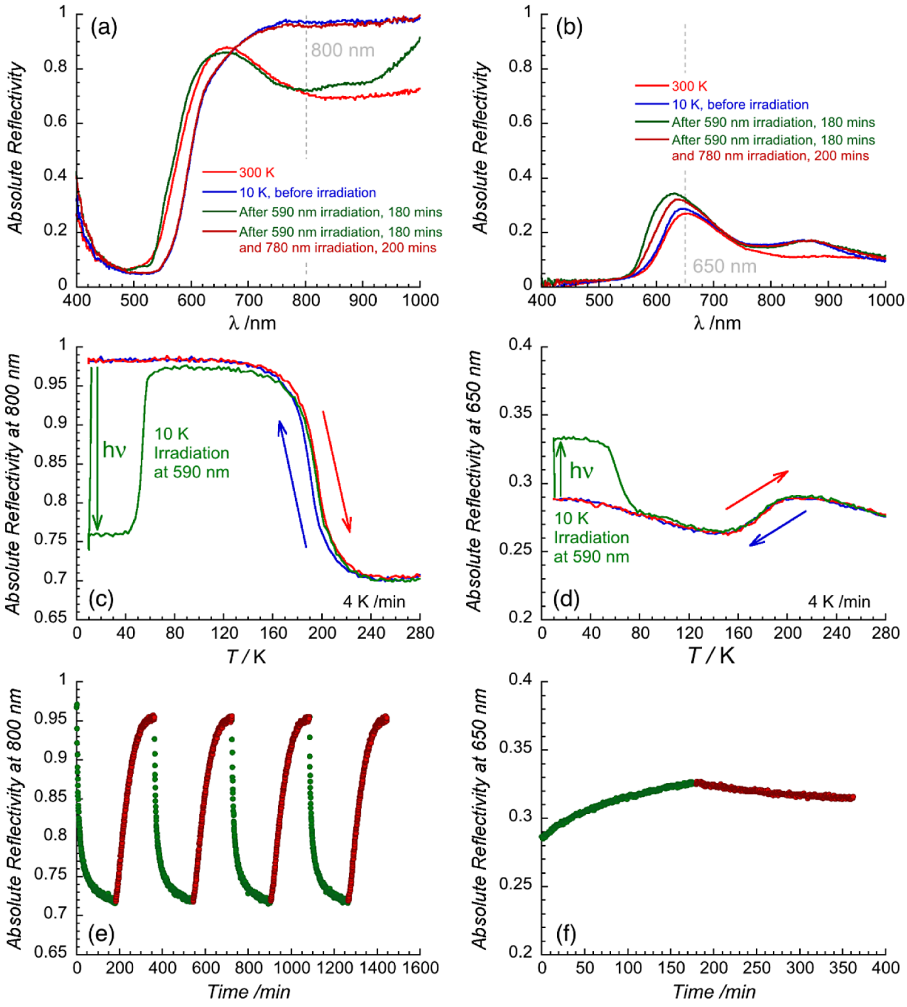

Figure 6. (a,b) Comparison of the optical reflectivity spectra at 300 K (red), 10 K before any irradiation (blue), after successive 180 min irradiation at 590 nm (green), and 200 min irradiation at 780 nm (dark red) for **1** (a; 1 mW cm^{-2}) and **2** (b; 1 mW cm^{-2}). (c,d) Thermal variation of the 800 nm (for **1**, c) and 650 nm (for **2**, d) optical reflectivity signals recorded at a scan rate of 4 K min^{-1} when cooling (blue trace) and heating (red trace) in the dark and when heating (green trace) after a 590 nm irradiation of 3 h at 10 K. A spectroscopic white light of 0.08 mW cm^{-2} has been used for these measurements. (e,f) Time evolution at 10 K of the reflectivity under successive irradiations of 590 nm (green dots, 1 mW cm^{-2}) and 780 nm (dark red dots, 1 mW cm^{-2}) showing optical reversibility of the spin state photoswitching at 800 nm for **1** (e) and 650 nm for **2** (f).

the χT product observed between 300 and 270 K is followed by an abrupt, in one step, decrease as the temperature is lowered to 150 K. Below this temperature, the remaining paramagnetism is small and reaches 0.037 cm^3 K mol^{-1} at 1.85 K, which corresponds to the presence of around 1% of residual HS Fe(II). This thermal behavior is characteristic of a complete SCO process centered around $T_{1/2}$ = 200 K in perfect agreement with the above structural, Mössbauer, and theoretical results. The temperature dependence of the χT product for **2** at 1 T is shown between 300 and 1.85 K in Figure 5c (gray dots). At RT, the χT value of 3.8 cm^3 K mol^{-1} is higher than that for **1** and the expected value for uncoupled S = 2 Fe(II) spins (3 cm^3 K mol^{-1}, g = 2). This result suggests that the average g value of the Fe sites in **2** is around 2.27 and thus is slightly higher than that found for **1**. As the temperature is reduced, χT remains constant until approximately 220 K and then undergoes a gradual decrease to a value of 2.8 cm^3 K mol^{-1} at 100 K in agreement with an incomplete SCO process centered around $T_{1/2}$ = 158 K. In most of the cases, this type of incomplete SCO is associated with the presence of multiple crystallographic Fe(II) centers, which do not all exhibit an SCO, or due to a local alteration of the Fe(II) surroundings, for example, when guest or solvent molecules are partially lost and induce the stabilization of HS Fe(II) sites.[56] In the case of **2**, which possesses a single crystallographic Fe site and no solvent of crystallization, the origin of this behavior is found in the bonding disorder of the 3acpy ligand (*vide supra*). As expected from the structural, Mössbauer, and theoretical data shown above, the χT decrease between 300 and 100 K corresponds to about 25% of the RT value in agreement with the presence of 25% of SCO Fe sites in a $[FeN_6]$ coordination sphere diluted into 75% of Fe centers ($[FeN_4O_2]$ and $[FeN_5O]$) that stay in their HS state. Thus, in **2**, only a gradual spin-crossover (*i.e.*, without a first-order phase transition) is observed as expected in highly diluted SCO material for which the elastic interactions between active $[FeN_6]$ sites cannot connect enough the dispersed SCO sites. Below 100 K, the χT product decreases significantly faster,

especially below 30 K, to a minimum value of 0.67 cm^3 K mol^{-1} at 1.85 K. This variation is the typical thermal signature of the HS Fe(II) magnetic anisotropy (*i.e.*, zero-field splitting) expected for HS $[FeN_4O_2]$ and $[FeN_5O]$ sites. As far as we know, **2** appears to be the first SCO material that exhibits an incomplete SCO due to a ligand coordination disorder at the Fe(II) sites, which induces three different Fe coordination spheres.

The magnetic susceptibility data of compounds **1** and **2** can be used to determine the thermodynamic parameters of the SCO process. The χT *vs* T plot of **1** and **2** (Figure 5) can be fitted to the ideal solution model (*i.e.*, without elastic interaction) using the following expression:[57]

$$\chi T = (\chi T)_{LT} + \frac{(\chi T)_{HT} - (\chi T)_{LT}}{1 + \exp\left(\frac{\Delta H}{R}\left(\frac{1}{T} - \frac{1}{T_{1/2}}\right)\right)}$$

with $(\chi T)_{LT}$ and $(\chi T)_{HT}$ being the limit values of the χT product at low and high temperatures, respectively, ΔH and $T_{1/2}$ are the enthalpy and the characteristic temperature of the SCO process. For **1**, the fitting of the experimental data (red solid line, Figure 5a) leads to ΔH = 34.9(4) kJ mol^{-1} and $T_{1/2}$ = 200(1) K allowing an estimation of the entropy associated with the SCO process, $\Delta S = \Delta H/T_{1/2}$ = 174 J K^{-1} mol^{-1}. In the case of **2**, a similar fit down to 50 K (red solid line, Figure 5c) leads to ΔH = 39(2) kJ mol^{-1} and $T_{1/2}$ = 157(2) K ($\Delta S = \Delta H/T_{1/2}$ = 254 J K^{-1} mol^{-1}) as well as 27(1)% of active SCO $[FeN_6]$ centers, in good agreement with the crystallographic results. The obtained thermodynamic values are perfectly consistent with those found for related SCO compounds[8,13] and confirm that both **1** and **2** do not display a spin-transition but a spin-crossover process (*i.e.*, without first-order phase transition).

Optical Reflectivity and Photomagnetic Properties. The thermo- and photochromism of the two reported complexes have been studied using optical reflectivity between 400 and 1000 nm (Figures 6, S12, and S13). At 300 K, the spectra of **1** and **2** are similar, showing weak reflectivity (*i.e.*, strong absorption) between 400 and 600 nm and then higher absolute reflectivity (AR) above 600 nm with a secondary minimum around 850 nm for **1** and 750 nm for **2**, attributed to the $d-d$ absorption of the HS Fe(II) centers (Figure 6a,b; red line).[32] Cooling from RT to 10 K causes an increase in the AR for both compounds above 700 nm, which can be attributed to the disappearance of some HS Fe(II) centers due to the thermally driven HS → LS SCO (blue traces in Figure 6a,b and red to blue traces in Figure S12) seen, for example, by magnetic measurements (Figure 5). The fact that this effect is substantially stronger for **1** than for **2** is probably associated with the complete *versus* incomplete (25%) SCO, respectively, observed. In other words, the reflectivity spectrum of **2** at 10 K is a combination of the optical spectra for the LS $[FeN_6]$ (25%) and HS $[FeN_5O]/[FeN_4O_2]$ (75%) sites. As observed by the magnetic measurements, the reflectivity spectra are perfectly reproducible in temperature when they are collected in cooling or heating modes; moreover, the initial and final RT spectra are fully superposed for both compounds (Figure S12c,d). Evidently, **1** and **2** exhibit a reversible thermochromic effect due to the reversible HS ↔ LS SCO process. Additionally, the AR with the highest optical contrast, at 800 nm for **1** and 650 nm for **2**, can be plotted between 280 and 10 K (4 K/min) in cooling and heating modes (Figure 6c,d; blue and red traces) to monitor the observed thermochromism. In the case of **1**, the change in the reflectivity signal is obvious between 240 and 160 K and is associated with the reversible HS ↔ LS SCO. Moreover, the fact that the AR at 800 nm is reaching a value near 1 at 120 K (Figure 6c) is in complete agreement with a full thermal conversion of the HS Fe(II) centers into their low-temperature LS state as observed in the magnetic, structural, and Mössbauer studies. Compared to **1**, the amplitude of the thermochromic effect on the optical reflectivity between 200 and 130 K (Figure 6d) for **2** is much weaker, as expected for a partial (25%) SCO process and a mixture of LS/HS Fe(II) sites at low temperatures.

As both compounds showed a clear thermochromism associated with a thermally induced SCO (Figures 6a–d and S12), the photoswitching of the HS ↔ LS SCO was tested at 10 K using a series of LEDs from 365 to 1050 nm.[58,59] As shown in Figure S13a,b, **1** and **2** exhibit significant photoactivity between 365 and 660 nm with a maximum response at 590 nm. Hence, photoconversion from the low-temperature state to the photoinduced HS state (HS*) was performed using this specific wavelength. When **1** and **2** are irradiated at 590 nm, the characteristic spectrum of the HS state (measured at 300 K) is recovered at 10 K after about 3 h (Figure 6a,b; green spectra) supporting a full photoconversion of the LS sites into HS* centers. When the temperature is subsequently increased, a complete thermal relaxation and thus a full reversibility are observed around 60 K for **1** and 80 K for **2** (Figure 6c,d; green spectra). Furthermore, the photoreversibility of the LS to HS* conversion at 10 K has also been tested by optical reflectivity. After a first irradiation at 590 nm (LS → HS*) at 10 K, the recovery of the LS spectra for **1** (HS* → LS) is obtained with a second irradiation between 735 and 940 nm (Figure S13c). Cycles of excitation at 590 nm and deexcitation at 780 nm have been performed for **1** at 10 K, and good photoswitchability is observed (Figure 6f). In contrast, while **2** can be photoexcited efficiently at 590 nm, the photoreversibility with a selected wavelength is not achieved (Figures 6e and S13d), and even using an irradiation at 780 nm like that for **1**, the reversibility is incomplete

The LS ↔ HS* photoswitching for the two reported compounds was also probed by photomagnetic measurements using the optical information gathered from the above reflectivity data. At 10 K, both materials were irradiated with a 590 nm light and measured under an applied magnetic field of 1 T. In both cases, a marked increase in the χT product at 10 K is observed in agreement with the photoconversion of diamagnetic Fe(II) sites into paramagnetic S = 2 Fe(II) centers (Figure 5). In the case of **1**, the χT value increases from 0.07 cm^3 mol^{-1} K to a maximum of 2.5 cm^3 mol^{-1} K after about 300 min of irradiation, while in the case of **2**, the χT value increases from 2.1 cm^3 mol^{-1} K to a maximum of 3.0 cm^3 mol^{-1} K after about 100 min of irradiation. After the irradiation was switched off, the temperature dependence of the photoinduced state was measured in the dark from 2 K (at 0.3 K min^{-1}). In both cases, the χT value first increases between 2 and 25 K as a signature of the HS Fe(II) magnetic anisotropy. At higher temperatures, the χT product decreases to reach a value measured before irradiation at 57 and 63 K for **1** and **2**, respectively (Figure 5a,c), *i.e.*, as expected, the Fe(II) sites in a metastable photoinduced HS* state relax to their LS ground state. Based on the amplitude of the χT variation upon photoexcitation at 590 nm (Figure 5), it seems that the LS Fe(II) sites in both compounds can be almost quantitatively photoconverted into

the HS* (S = 2) centers. Similarly to the reflectivity studies (Figure 6e,f), the reversible switchability of the LS ↔ HS* conversion was probed by measuring the magnetic susceptibility over cycles of consecutive 590 nm (LS → HS*)/780 nm (HS* → LS) irradiations at 10 K and with a 1 T applied field (Figure 5b,d). These magnetic measurements confirm the conclusions of the optical reflectivity studies, which demonstrated that (i) **1** can be reversible and quantitatively photoconverted over several excitation−deexcitation cycles without showing significant fatigue over time, while (ii) **2** shows poor photoswitchability. The presence of only 25% of SCO [FeN_6] sites diluted into 75% of HS sites impacts the photoactivity of **2** and the reversibility of the phenomenon. When LS [FeN_6] sites are photoconverted into HS* [FeN_6] sites, the weak elastic interactions between active-dispersed [FeN_6] sites cannot help the reverse HS* → LS photoconversion, and indeed the [FeN_6] sites prefer to remain in their HS* state as the majority (75%) of the surrounding sites are inactive HS sites.

General Discussion. As mentioned in the Introduction, several 2D Hofmann CPs belonging to the family of the {Fe(nR-py)$_2$[Ag(CN)$_2$]$_2$} compounds are reported in the literature. The simplest compound {Fe(py)$_2$[Ag(CN)$_2$]$_2$}[13,15] exhibits square grid {Fe[Ag(CN)$_2$]$_2$} layers interacting through weak pyridine−pyridine interactions with an incomplete two-step SCO and low $T_{1/2}$ temperatures (<150 K). When the pyridine ring is functionalized by alkyl substituents, $\pi\cdots\pi$ interactions are weakened due to steric hindrance and, in some cases, the supramolecular packing is dominated by argentophilic interactions.[16] When cyanido[19] or aromatic[14] substituents are used, the final materials display higher $T_{1/2}$ and complete SCO. The 2D Hofmann CPs with 3X-pyridine (X = F, Cl, Br, or I) ligands, {Fe(3X-py)$_2$[M(CN)$_2$]$_2$}, present systematically metallophilic interactions, but the SCO process is completely lost in the systems with the heavier halides (Br^- and I^-), while the materials with the lighter F^- ($T_{1/2}$ = 162 K/96 K) and Cl^- ($T_{1/2}$ = 106 K) show incomplete SCO.[15,17] These results strongly suggest that the metallophilic interactions cannot explain on their own the presence (complete or incomplete) or the absence of an SCO. It is worth mentioning that Galet *et al.* reported a completely new structure with 3-cyanopyridine and dominating argentophilic interactions.[18] In this case, the usual 2D architecture is replaced by a triple interpenetrated structure with a novel triangular Ag_3 motif, which leads to a one-step, complete SCO with a $T_{1/2}$ of 187 K. This example is similar to **2** for which the coordination of the iron centers to the ketone groups induces a loss of the classical 2D {Fe[Ag(CN)$_2$]$_2$} grid and the formation of a 3D structure with interconnected [Fe(3acpy)]$^{2+}$ and [Ag(CN)$_2$]$_2^{2-}$ chains (Figure 2). The discrete Ag_3-triangle reported by Galet *et al.*[18] is also observed in the [Ag(CN)$_2$]$_2^{2-}$ chain and was previously reported in similar frameworks, for example, forming {[Ag(CN)$_2$][Ag(CN)$_2$]}$_n^{2-}$ chains in which the Ag_3-triangles are supported by μ-CN^- bridges due to the *in situ* formation of dimeric [$Ag_2(CN)_3$]$^-$ units.[60] The lack of cyanido connectivity between the silver cations within the [Ag(CN)$_2$]$_2^{2-}$ chains makes the Ag_3 triangular moiety in **2** the first example of ligand-unsupported argentophilic interactions observed in Fe(II)−Ag(I) cyanido frameworks.[61]

As far as we know, there are only two reported examples of an {Fe(nR-py)$_2$[Ag(CN)$_2$]$_2$} compound with nR-substituents showing a terminal *O*-coordination. Both have been reported by Kosone *et al.*[19] When using allylisonicotinate and benzylnicotinate ligands, the final materials display a complete two-step SCO process (between 230 and 217 K and between 260 and 208 K, respectively).

Additionally, two other related examples should be mentioned replacing the nR-pyridine ligand with 2-ethoxypyrazine[62] or 4-methoxypyrimidine.[63] The {Fe(2-ethoxypyrazine)$_2$[Ag(CN)$_2$]$_2$} compound shows a remarkable four-step SCO (between 260 and 120 K), while {Fe(4-methoxypyrimidine)$_2$[M(CN)$_2$]$_2$} displays only HS Fe(II) sites. It is worth mentioning that a stepwise SCO process can be obtained only when 4-methoxypyrimidine or 4,6-dimethoxypyrimidine molecules cocrystallize with the {Fe(4-methoxypyrimidine)$_2$[M(CN)$_2$]$_2$} network. Both compounds, free of guest molecules, maintain the {Fe[Ag(CN)$_2$]$_2$} grid 2D network that resembles the triple interlocked structure of **1** with the substituted pyrazine/pyrimidine accommodated in the square window of the grid. Although in each case the *O*-donor alkoxy groups are pointing out to the Ag(I) cations in a manner that is reminiscent of what is seen in **1** (*vide supra*), the longer Ag···O distances suggest that in these cases the interaction is weaker. In fact, the main supramolecular interactions in the stacking of the layers are argentophilic interactions in the case of {Fe(2-ethoxypyrazine)$_2$[Ag(CN)$_2$]$_2$} and Ag···N/$\pi\cdots\pi$ interactions in the case of {Fe(4-methoxypyrimidine)$_2$[M(CN)$_2$]$_2$}. The above discussion shows the key importance of the supramolecular interactions in 2D {Fe(nR-py)$_2$[Ag(CN)$_2$]$_2$} Hofmann CPs offering opportunities to design new coordination polymers with tunable SCO.

Finally, the photoswitching of the SCO process has been reported for only a few examples of {Fe(nR-py)$_2$[Ag(CN)$_2$]$_2$} compounds, but none of them show a complete and reversible optical and photomagnetic conversion. In this context, the efficient and quantitative photoswitching of **1** over various excitation−deexcitation cycles without significant fatigue (Figures 5b and 6e) is relatively unique and opens interesting perspectives for thermo- and photoswitching applications.

In summary, two new cyanido-bridged Fe(II)−Ag(I) coordination polymers exhibiting thermochromism and SCO have been synthesized. The obtained crystal structures and their associated SCO properties are dictated by the choice of acetylpyridine ligand and the acetyl group position. When using the 4-acetylpyridine in **1**, a typical 2D Hofmann coordination polymer is obtained with interlayer interactions dominated by silver−ketone supramolecular contacts. This crystal structure stabilizes a complete and reversible SCO in temperature with $T_{1/2}$ = 200 K. In **2**, an unexpected coordination of the 3-acetylpyridine ligand is observed with the carbonyl group coordinating the Fe(II) sites, which induces the formation of (i) dicyanidoargentate chains with argentophilic interactions, (ii) [Fe(3acpy)]$^{2+}$ zigzag chains, and (iii) a 3D structure interconnecting the [Ag(CN)$_2$]$_2^{2-}$ and Fe/3acpy chains. Furthermore, the disorder of the 3-acetylpyridine ligand induces a disorder in the Fe(II) coordination sphere, leading to three possible Fe(II) chemical environments ([N_6], [N_4O_2], and [N_5O]) in **2**. This structural feature induces an incomplete SCO (25%) related to the statistical presence of 25% [FeN_6] sites. Moreover, both compounds are photosensitive and exhibit photomagnetic properties. It is worth highlighting that **1** shows quantitative and fully reversible photoswitching of the SCO properties.

These materials and their characterizations provide precious new information for a rational design of future structural arrangements directed by supramolecular interactions in order to allow a fine-tuning of the thermally and photoinduced SCO properties in the family of iron(II)−silver(I) cyanido-bridged coordination polymers.

C.C. acknowledges the financial support of ANID FONDECYT Iniciación *N*°11241257 and ANID FONDECYT Postdoctorado *N*°3210314. V.P.-G. acknowledges ANID FONDECYT Regular *N*°1211394. L.C.-G. and S.E.R.-L. acknowledge support from ANID FONDECYT Regular *N*°1220986. N.A. acknowledges Dr. T. Roisnel from CDIFX (Centre de Diffractométrie X), UMR CNRS 6226 Rennes, for single-crystal X-ray data collection. N.M. acknowledges financial support provided by the Spanish Ministry of Science and Innovation through the project PID2021-123431OB-I00. R.C., C.M., and M.R. acknowledge the support of the University of Bordeaux, the Région Nouvelle-Aquitaine, Quantum Matter Bordeaux (QMBx), and the Centre National de la Recherche Scientifique (CNRS). The authors acknowledge CONICYT-FONDEQUIP/PPMS/EQM130086-UNAB, French-Chilean International Research Project "Cooperation in Inorganic Chemistry" (CoopIC), Financiamiento Basal AFB220001 CEDENNA, and Laboratorio de Análisis de Sólidos (L.A.S-UNAB). Theory work was performed at The Molecular Foundry, which is supported by the Office of Science, Office of Basic Energy Sciences of the U.S. Department of Energy under Contract DE-AC02-05CH11231. Powered@NLHPC: This research was partially supported by the supercomputing infrastructure of NLHPC (Grant ECM-02).

(1) Gütlich, P.; Goodwin, H. A. Spin Crossover—An Overall Perspective. *Top. Curr. Chem.* **2004**, *233*, 1−47.
(2) Manrique-Juárez, M. D.; Rat, S.; Salmon, L.; Molnár, G.; Quintero, C. M.; Nicu, L.; Shepherd, H. J.; Bousseksou, A. Switchable Molecule-Based Materials for Micro- and Nanoscale Actuating Applications: Achievements and Prospects. *Coord. Chem. Rev.* **2016**, *308*, 395−408.
(3) Létard, J. F.; Guionneau, P.; Goux-Capes, L. Towards Spin Crossover Applications. *Top. Curr. Chem.* **2004**, *235*, 221−249.
(4) Nihei, M.; Shiga, T.; Maeda, Y.; Oshio, H. Spin Crossover Iron(III) Complexes. *Coord. Chem. Rev.* **2007**, *251*, 2606−2621.
(5) Weber, B. Spin Crossover Complexes with N_4O_2 Coordination Sphere - The Influence of Covalent Linkers on Cooperative Interactions. *Coord. Chem. Rev.* **2009**, *253*, 2432−2449.
(6) Senthil Kumar, K.; Ruben, M. Emerging Trends in Spin Crossover (SCO) Based Functional Materials and Devices. *Coord. Chem. Rev.* **2017**, *346*, 176−205.
(7) Powell, H. M.; Rayner, J. H. Clathrate Compound Formed by Benzene with an Ammonia−Nickel Cyanide Complex. *Nature* **1949**, *163*, 566−567.

(8) Muñoz, M. C.; Real, J. A. Thermo-, Piezo-, Photo- and Chemo-Switchable Spin Crossover Iron(II)-Metallocyanate Based Coordination Polymers. *Coord. Chem. Rev.* **2011**, *255*, 2068−2093.
(9) Garcia, Y.; Niel, V.; Muñoz, M. C.; Real, J. A. Spin Crossover in 1D, 2D and 3D Polymeric Fe(II) Networks. *Top. Curr. Chem.* **2004**, *233*, 229−257.
(10) Shylin, S. I.; Kucheriv, O. I.; Shova, S.; Ksenofontov, V.; Tremel, W.; Gural'skiy, I. A. Hofmann-Like Frameworks Fe(2-methylpyrazine)$_n$[M(CN)$_2$]$_2$ (M = Au, Ag): Spin-Crossover Defined by the Precious Metal. *Inorg. Chem.* **2020**, *59*, 6541−6549.
(11) Ohba, M.; Yoneda, K.; Agustí, G.; Muñoz, M. C.; Gaspar, A.; Real, J. A.; Yamasaki, M.; Ando, H.; Nakao, Y.; Sakaki, S.; Kitagawa, S. Bidirectional Chemo-Switching of Spin State in a Microporous Framework. *Angew. Chem., Int. Ed.* **2009**, *48*, 4767−4771.
(12) Valverde-Muñoz, F. J.; Bartual-Murgui, C.; Piñeiro-López, L.; Muñoz, M. C.; Real, J. A. Influence of Host-Guest and Host-Host Interactions on the Spin-Crossover 3D Hofmann-Type Clathrates {Fe^{II}(*pina*)[M^{I}(CN)$_2$]$_2$}·*x*MeOH (M^{I} = Ag, Au). *Inorg. Chem.* **2019**, *58*, 10038−10046.
(13) Rodíguez-Velamán, J. A.; Castro, M.; Palacios, E.; Burriel, R.; Kitazawa, T.; Kawasaki, T. A Two-Step Spin Transition with a Disordered Intermediate State in a New Two-Dimensional Coordination Polymer. *J. Phys. Chem. B* **2007**, *111*, 1256−1261.
(14) Wang, L. F.; Zhuang, W. M.; Huang, G. Z.; Chen, Y. C.; Qiu, J. Z.; Ni, Z. P.; Tong, M. L. Spin-Crossover Modulation *Via* Single-Crystal to Single-Crystal Photochemical [2 + 2] Reaction in Hofmann-Type Frameworks. *Chem. Sci.* **2019**, *10*, 7496−7502.
(15) Rodríguez-Velamazán, J. A.; Carbonera, C.; Castro, M.; Palacios, E.; Kitazawa, T.; Létard, J. F.; Burriel, R. Two-Step Thermal Spin Transition and LIESST Relaxation of the Polymeric Spin-Crossover Compounds Fe(X-py)$_2$[Ag(CN)$_2$]$_2$ (X = H, 3-methyl, 4-methyl, 3,4-dimethyl, 3-Cl). *Chem.-Eur. J.* **2010**, *16*, 8785−8796.
(16) Rodríguez-Velamazán, J. A.; Kitase, K.; Palacios, E.; Castro, M.; Fernández-Blanco, Á.; Burriel, R.; Kitazawa, T. Structural Insights into the Two-Step Spin-Crossover Compound Fe(3,4-dimethylpyridine)$_2$[Ag(CN)$_2$]$_2$. *Crystals* **2019**, *9*, 316.
(17) Muñoz, M. C.; Gaspar, A. B.; Galet, A.; Real, J. A. Spin-Crossover Behavior in Cyanide-Bridged Iron(II)-Silver(I) Bimetallic 2D Hofmann-like Metal-Organic Frameworks. *Inorg. Chem.* **2007**, *46*, 8182−8192.
(18) Galet, A.; Niel, V.; Muñoz, M. C.; Real, J. A. Synergy between Spin Crossover and Metallophilicity in Triple Interpenetrated 3D Nets with the NbO Structure Type. *J. Am. Chem. Soc.* **2003**, *125*, 14224−14225.
(19) Kosone, T.; Makido, Y.; Okuda, S.; Haigo, A.; Kawasaki, T.; Akahoshi, D.; Saito, T.; Kitazawa, T. Systematic Design of Crystal Structure for Hofmann-like Spin Crossover Fe(L)$_2$[Ag(CN)$_2$]$_2$ Complexes. *Crystals* **2019**, *9*, 370.
(20) Kucheriv, O. I.; Shylin, S. I.; Ksenofontov, V.; Dechert, S.; Haukka, M.; Fritsky, I. O.; Guralskiy, I. A. Spin Crossover in Fe(II)−M(II) Cyanoheterobimetallic Frameworks (M = Ni, Pd, Pt) with 2-Substituted Pyrazines. *Inorg. Chem.* **2016**, *55* (10), 4906−4914.
(21) Niel, V.; Thompson, A. L.; Muñoz, M. C.; Galet, A.; Goeta, A. E.; Real, J. A. Crystalline-State Reaction with Allosteric Effect in Spin-Crossover, Interpenetrated Networks with Magnetic and Optical Bistability. *Angew. Chem., Int. Ed.* **2003**, *42* (32), 3760−3763.
(22) Kitase, K.; Akahoshi, D.; Kitazawa, T. Effects of Both Methyl and Pyrimidine Groups in Fe−Ag Spin-Crossover Hofmann-Type Complex {Fe(4-Methylpyrimidine) $_2$[Ag(CN)$_2$]$_2$}. *Inorg. Chem.* **2021**, *60* (7), 4717−4722.
(23) *SAINT V6.22. SAINT V6.22 Bruker AXS Inc.*; Bruker AXS Inc: Madison, WI, USA, 2000.
(24) *SADABS V2.05. SADABS V2.05 Bruker AXS Inc.*; Bruker AXS Inc.: Madison, WI, USA, 2001.
(25) Dolomanov, O. V.; Bourhis, L. J.; Gildea, R. J.; Howard, J. A. K.; Puschmann, H. OLEX2: A Complete Structure Solution, Refinement and Analysis Program. *J. Appl. Crystallogr.* **2009**, *42*, 339−341.
(26) Sheldrick, G. M. SHELXT - Integrated Space-Group and Crystal-Structure Determination. *Acta Crystallogr., Sect. A: found. Adv.* **2015**, *A71*, 3−8.
(27) Sheldrick, G. M. Crystal Structure Refinement with SHELXL. *Acta Crystallogr., Sect. C: Struct. Chem.* **2015**, *C71*, 3−8.
(28) Blatov, V.; Shevchenko, A. Program Package for Multipurpose Crystallochemical Analysis. ToposPro V5.0; 2001.
(29) Blanton, J. R.; Papoular, R. J.; Louër, D. PreDICT: A Graphical User Interface to the DICVOL14 Indexing Software Program for Powder Diffraction Data. *Powder Diffr.* **2019**, *34*, 233−241.
(30) Rodríguez-Carvajal, J.; Roisnel, T. Line Broadening Analysis Using Fullprof: Determination of Microestructural Properties. *Mater. Sci. Forum.* **2004**, *443−444*, 123−126.
(31) Roisnel, T.; Rodríguez-Carvajal, J. WinPLOT: A Windows Tool for Powder Diffraction Pattern Analysis. *Mater. Sci. Forum.* **2001**, *378−381*, 118−123.
(32) Ye, Y. S.; Chen, X. Q.; Cai, Y. D.; Fei, B.; Dechambenoit, P.; Rouzières, M.; Mathonière, C.; Clérac, R.; Bao, X. Slow Dynamics of the Spin-Crossover Process in an Apparent High-Spin Mononuclear Fe^{II} Complex. *Angew. Chem., Int. Ed.* **2019**, *58* (52), 18888−18891.
(33) Brand, R. A. Improving the Validity of Hyperfine Field Distributions from Magnetic Alloys: Part I: Unpolarized Source. *Nucl. Instrum. Methods Phys. Res.* **1987**, *B28*, 398−416.
(34) Kresse, G.; Furthmüller, J. Efficient Iterative Schemes for Ab Initio Total-Energy Calculations Using a Plane-Wave Basis Set. *Phys. Rev. B* **1996**, *54*, 11169−11186.
(35) Kresse, G.; Furthmüller, J. Efficiency of Ab-Initio Total Energy Calculations for Metals and Semiconductors Using a Plane-Wave Basis Set. *Comput. Mater. Sci.* **1996**, *6*, 15−50.
(36) Perdew, J. P.; Ruzsinszky, A.; Csonka, G. I.; Vydrov, O. A.; Scuseria, G. E.; Constantin, L. A.; Zhou, X.; Burke, K. Restoring the Density-Gradient Expansion for Exchange in Solids and Surfaces. *Phys. Rev. Lett.* **2008**, *100*, 136406.
(37) Dudarev, S.; Botton, G.; Savrasov, S. Y. C.; Humphreys, J.; Sutton, A. P. Electron-Energy-Loss Spectra and the Structural Stability of Nickel Oxide: An LSDA+U Study. *Phys. Rev. B* **1998**, *57*, 1505−1509.
(38) Cococcioni, M.; de Gironcoli, S. Linear Response Approach to the Calculation of the Effective Interaction Parameters in the LDA+U Method. *Phys. Rev. B* **2005**, *71*, 035105.
(39) Wang, L.; Maxisch, T.; Ceder, G. Oxidation Energies of Transition Metal Oxides within the GGA+U Framework. *Phys. Rev. B* **2006**, *73*, 195107.
(40) Zhou, F.; Cococcioni, M.; Marianetti, C. A.; Morgan, D.; Ceder, G. First-Principles Prediction of Redox Potentials in Transition-Metal Compounds with LDA + U. *Phys. Rev. B* **2004**, *70*, 235121.
(41) Kresse, G.; Joubert, D. From Ultrasoft Pseudopotentials to the Projector Augmented-Wave Method. *Phys. Rev. B* **1999**, *59*, 1758−1775.
(42) Llunell, M.; Casanova, D.; Cirera, J.; Bofill, J.; Alemany, P.; Alvarez, S.; Pinsky, M.; Avnir, D. S. *SHAPE V2.1 2013, Universitat de Barcelona, Barcelona. This program has been developed in the group of Prof.* Alvarez at the Universitat de Barcelona and is available from the authors at llunell@qf.ub.es).
(43) Ketkaew, R.; Tantirungrotechai, Y.; Harding, P.; Chastanet, G.; Guionneau, P.; Marchivie, M.; Harding, D. J. A Tool for Calculating Distortion Parameters in Spin Crossover and Coordination Complexes. *Dalton Trans.* **2021**, *50* (3), 1086.
(44) Halcrow, M. A. Structure: Function relationships in molecular spin-crossover complexes. *Chem. Soc. Rev.* **2011**, *40* (7), 4119−4142.
(45) Agustí, G.; Muñoz, M. C.; Gaspar, A. B.; Real, J. A. Spin-Crossover Behavior in Cyanide-Bridged Iron(II)-Gold(I) Bimetallic 2D Hofmann-like Metal-Organic Frameworks. *Inorg. Chem.* **2008**, *47*, 2552−2561.
(46) Benaissa, H.; Rotaru, A.; Garcia, Y. Spin Crossover in Two 1D Fe(II) Polymers with 1,2,4-Triazole Thiourea Building Blocks. *Hyperfine Interact.* **2018**, *239*, 37.

(47) Phonsri, W.; Davies, C. G.; Jameson, G. N. L.; Moubaraki, B.; Ward, J. S.; Kruger, P. E.; Chastanet, G.; Murray, K. S. Symmetry Breaking above Room Temperature in an Fe(II) Spin Crossover Complex with an N_4O_2 Donor Set. *Chem. Commun.* **2017**, *53*, 1374−1377.
(48) Weber, B.; Kaps, E.; Weigand, J.; Carbonera, C.; Létard, J. F.; Achterhold, K.; Parak, F. G. Cooperative Iron(II) Spin Crossover Complexes with N_4O_2 Coordination Sphere. *Inorg. Chem.* **2008**, *47*, 487−496.
(49) Salmon, L.; Bousseksou, A.; Donnadieu, B.; Tuchagues, J. P. Two Novel Iron(II) Materials Based on Dianionic N_4O_2 Schiff Bases: Structural Properties and Spin-Crossover Characteristics in the Series [Fe(3-X,5-NO_2-sal-N(1,4,7,10)] (X = H, 3-MeO, 3-EtO). *Inorg. Chem.* **2005**, *44*, 1763−1773.
(50) Moliner, N.; Munoz, C.; Létard, S.; Solans, X.; Menendez, N.; Goujon, A.; Varret, F.; Real, J. A. Spin Crossover Bistability in Three Mutually Perpendicular Interpenetrated (4,4) Nets. *Inorg. Chem.* **2000**, *39*, 5390−5393.
(51) Vela, S.; Fumanal, M.; Cirera, J.; Ribas-Arino, J. Thermal Spin Crossover in Fe(II) and Fe(III). Accurate Spin State Energetics at the Solid State. *Phys. Chem. Chem. Phys.* **2020**, *22*, 4938−4945.
(52) Vela, S.; Fumanal, M.; Ribas-Arino, J.; Robert, V. Towards an Accurate and Computationally-Efficient Modelling of Fe(II)-Based Spin Crossover Materials. *Phys. Chem. Chem. Phys.* **2015**, *17*, 16306−16314.
(53) Zhang, Y. Predicting Critical Temperatures of Iron(II) Spin Crossover Materials: Density Functional Theory plus U Approach. *J. Chem. Phys.* **2014**, *141*, 214703.
(54) Paulsen, H. Periodic Density Functional Calculations in Order to Assess the Cooperativity of the Spin Transition in Fe(phen)$_2$(NCS)$_2$. *Magnetochemistry* **2016**, *2*, 14.
(55) Aravena, D.; Castillo, Z. A.; Muñoz, M. C.; Gaspar, A. B.; Yoneda, K.; Ohtani, R.; Mishima, A.; Kitagawa, S.; Ohba, M.; Real, J. A.; Ruiz, E. Guest Modulation of Spin-Crossover Transition Temperature in a Porous Iron(II) Metal-Organic Framework: Experimental and Periodic DFT Studies. *Chem.-Eur. J.* **2014**, *20*, 12864−12873.
(56) Shatruk, M.; Phan, H.; Chrisostomo, B. A.; Suleimenova, A. Symmetry-Breaking Structural Phase Transitions in Spin Crossover Complexes. *Coord. Chem. Rev.* **2015**, *289−290*, 62−73.
(57) Atkins, P.; De Paula, J. *Physical Chemistry*, 8th, ed.; Oxford University Press, 2006.
(58) Chastanet, G.; Desplanches, C.; Gonidec, M.; Guionneau, P.; Marchivie, M.; Mathonière, C.; Rosa, P. Light-Induced Excited Spin-State Trapping: A Methodological Approach. In *Comprehensive Coordination Chemistry III*. 2021, 198-216.
(59) Morscheidt, W.; Jeftic, J.; Codjovi, E.; Linares, J.; Bousseksou, A.; Constant-Machado, H.; Varret, F. Optical Detection of the Spin Transition by Reflectivity: Application to $[Fe_xCo_{1-x}(btr)_2(NCS)_2]\cdot H_2O$. *Meas. Sci. Technol.* **1988**, 1311−1315.
(60) Kosone, T.; Suzuki, Y.; Ono, S.; Kanadani, C.; Saito, T.; Kitazawa, T. A New Spin Crossover Heterometallic $Fe^{II}Ag^{I}$ Coordination Polymer with the $[Ag_2(CN)_3]^-$ Unit: Crystallographic and Magnetic Study. *Dalton Trans.* **2010**, *39*, 1786−1790.
(61) Schmidbaur, H.; Schier, A. Argentophilic Interactions. *Angew. Chem., Int. Ed.* **2015**, *54*, 746−784.
(62) Kucheriv, O.; Shylin, S. I.; Sirenko, V. Y.; Ksenofontov, V.; Tremel, W.; Dasčlu I, A.; Shova, S.; Gural'skiy, I. A. Four-Step Spin Crossover in a New Cyano-Bridged Iron-Silver Coordination Polymer. *Chem.-Eur. J.* **2022**, *28*, No. e202200924.
(63) Kitase, K.; Akahoshib, D.; Kitazawa, T. Guest-triggered "Soma−Iwamoto-type" penetration complex {Fe(4-methoxypyrimidine)$_2$[M(CN)$_2$]$_2$}·Guest (M = Ag, Au). *Dalton Trans.* **2023**, *52* (9), 2571−2579.

Thermally- and Photo-Induced Spin-Crossover Behavior in Iron(II)−Silver(I) Cyanido-Bridged Coordination Polymers Bearing Acetylpyridine Ligands

Carlos Cruz,[a,b] Jorge Galdames,[a,b] Liz Camayo-Gutierrez,[c] Mathieu Rouzières,[d] Corine Mathonière,[d] Nieves Menéndez,[e] Nathalie Audebrand,[f] Sebastian E. Reyes-Lillo,[g] Rodolphe Clérac,*[d] Diego Venegas-Yazigi,[b,h] Verónica Paredes-García*[a,b]*

1. Synthetical and characterization details

Pure orange powder samples of **1** and **2** can be obtained directly by reacting 0.5 mmol of $Fe(ClO_4)_2 \cdot xH_2O$ and 1 mmol of *n*-acetylpyridine (*n* = 3 for **1** and *n* = 4 for **2**) dissolved in 10 mL of 1:1 water-ethanol solution with a water solution (10 mL) of $K[Ag(CN)_2]$ (1 mmol). Yield of 42% for **1** and 51% for **2**.

Dark orange single crystals of **1** and **2** were obtained by different slow diffusion techniques using a 1:1 water-ethanol solution of $Fe(ClO_4)_2 \cdot xH_2O$ (1 mmol) and *n*-acetylpyridine (2 mmol; *n* = 4 for **1** and *n* = 3 for **2**) and a water solution of $K[Ag(CN)_2]$ (2 mmol):

(a) A 3 mL straight tube was filled with 500 µL of the $K[Ag(CN)_2]$ water solution, 1000 µL of 2:1 water-ethanol as buffer intermediate layer, and a superior layer of 500 µL of the $Fe(ClO_4)_2$/*n*-acetylpyridine solution. The filled tube was closed with paraffin film. Single crystals are obtained after two days of crystallization. Yield of 26% for **1** and 31% for **2**.

(b) One side of a 20 mL H-shape tube was filled with 5 mL of the $Fe(ClO_4)_2$/*n*-acetylpyridine solution. 5 mL of a $K[Ag(CN)_2]$ water solution was placed on the other side of the H-tube. Pure ethanol or 1:1 water-ethanol solutions were used as a top layer to connect the two compartiments of the H-tube, which were closed by a screw cap. Single crystal are obtained after one week of crystallization. Yield of 38% for **1** and 46% for **2**.

(c) A 3 mL vial filled with 2 mL of the $Fe(ClO_4)_2$/*n*-acetylpyridine solution was introduced in a 20 mL vial containing 3 mL of the $K[Ag(CN)_2]$ water solution. Both vessels were filled with pure ethanol or a water-ethanol solution, and the 20 mL vial was closed with a screw cap. Single crystal are obtained after one week of crystallization. Yield of 29% for **1** and 40% for **2**.

Thermogravimetric Analysis

Thermograms of **1** and **2** (Figure S2) show that both compounds present thermal stability in air atmosphere until approximately 200°C. From this point, the total decomposition is approximately achieved around 400°C for both compounds.

FTIR Spectroscopy

FTIR-ATR (cm^{-1}) for **1 =** 2161(w), 2115(vw), 1689(s), 1652(vw), 1606(vw), 1556(vw),1412(w), 1362(w), 1338(vw), 1321(vw), 1264(m), 1253(m), 1225(vw), 1212(vw), 1086(vw), 1060(vw), 1012(vw), 961(vw), 874(vw), 823(vs), 746(vw), 592(s), 438(w).

FTIR-ATR (cm^{-1}) for **2 =** 2161(w), 1671(w), 1642(vw), 1590(w), 1553(vw), 1476(vw), 1426(vw), 1363(vw), 1326(vw), 1282(w), 1253(vw), 1201(vw), 1131(vw), 1097(vw), 1081(vw), 1043(vw), 1032(vw), 1016(vw), 962(vw), 813(w), 760(vw), 695(w), 642(vw), 592(vw), 498(vw), 485(vw), 435(w).

The IR pattern of **1** and **2** show a clear resemblance to the one of the free ligands (Figure S3). Compounds **1** and **2** display the characteristic $\overline{\nu}$(C=O) vibration of the ketone group at 1689 and 1671 cm^{-1}, respectively. These IR bands show a subtle shift with respect to the free ligand at 1693 and 1685 cm^{-1} for 4acpy and 3acpy respectively (Δ_1 = 4 cm^{-1} and Δ_2 = 14 cm^{-1}). The fact that the Δ_2 is greater than Δ_1 suggests that the carbonyl of 3acpy may be coordinated to the metal ions in the structure of **2** while in **1** it should present as free carbonyl. Additionally, in both cases the characteristic $\overline{\nu}$(C≡N) is found at 2161 cm^{-1}, confirming the existence of $[Ag(CN)_2]^-$ fragment in the structures of **1** and **2**.

Energy dispersive Spectroscopy

% Ratio between Fe and Ag were evaluated by EDXS (Figure S4). Compound **1** presents a 19.11 wt.% and 39.87 wt.% for Fe and Ag, respectively, and **2** presents a 17.61 wt.% and 38.19 wt.% for Fe and Ag. In both cases, the 1:2 ratio of Fe:Ag is confirmed.

2. Supplementary figures.

Figure S1. Le Bail fits of the powder diffraction patterns of samples **1** (a) and **2** (b) collected at 293 K and refined unit-cell parameters.

Figure S2. Thermograms of **1** and **2**.

Figure S3. Infrared spectra of **1** and 4-acetylpyridine and of **2** and 3-acetylpyridine.

Figure S4. EDXS analysis for **1** and **2**.

Figure S5. Additional views of the crystal structures of **1**.

Figure S6. Additional views of the crystal structures of **2**.

Figure S7. ^{57}Fe Mössbauer spectra for **1** at 150 K, 210 K and 290 K.

Figure S8. Thermal Evolution of the isomer shift (δ) and the quadrupole splitting (ΔE_Q) for **2**.

Figure S9-10. DFT+U calculations for **1** and **2**.

Figure S11. Schematic unit cell of the two theoretical models for **2** used for the DFT+U calculations.

Figure S12. Optical reflectivity spectra at selected temperatures decreasing the temperature from 300 to 10 K (a & b) and increasing the temperature from 10 K to room temperature (c & d) for **1** (a,c) and **2** (b,d).

Figure S13. Variation of the absolute optical reflectivity at 10 K for **1** and **2** (i) comparing before and after excitation with different LEDs; (ii) comparing after a 590-nm irradiation of the sample and after desexcitation with different LEDs.

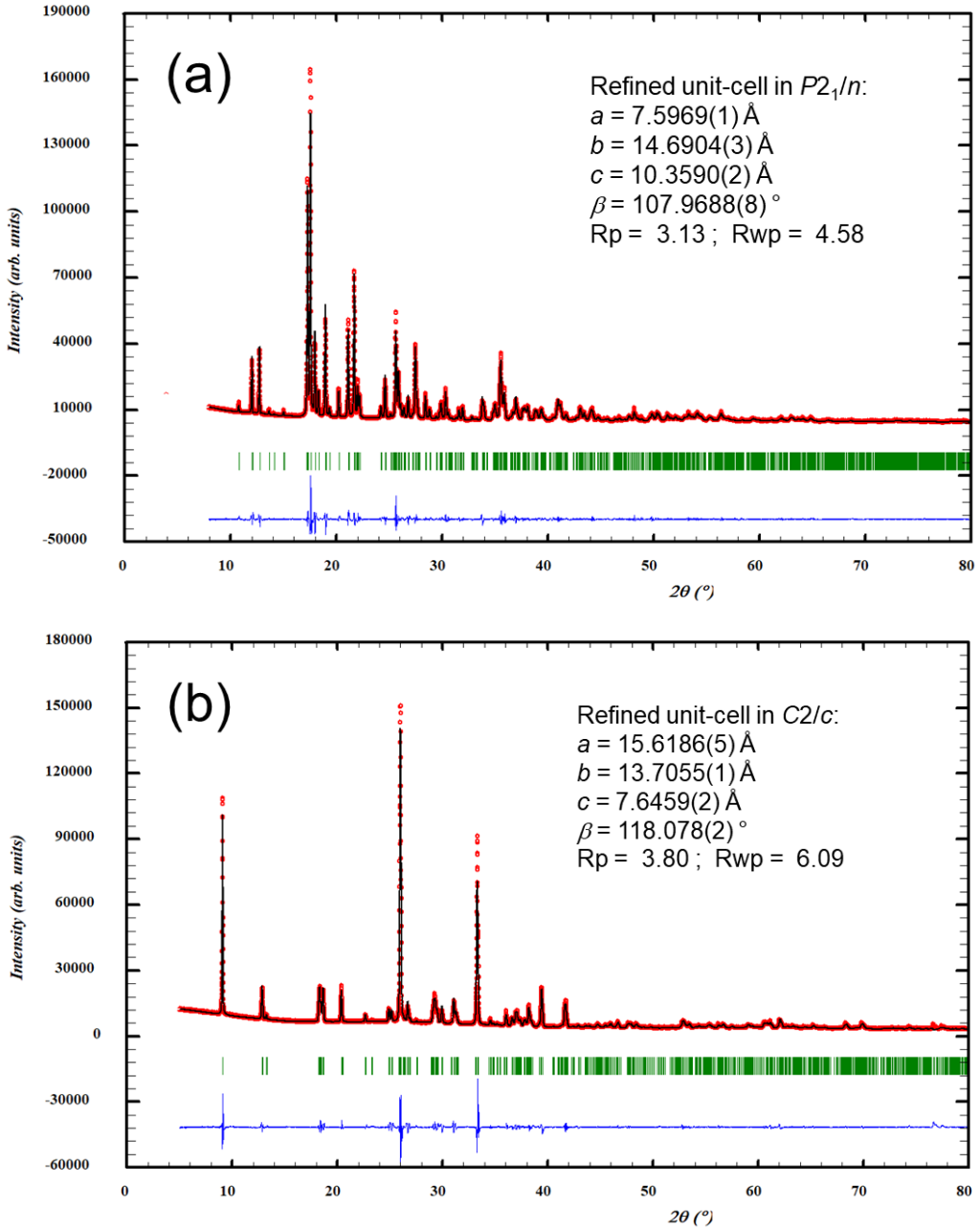

Figure S1. Le Bail fits of the powder diffraction patterns of samples **1** (a) and **2** (b) collected at 293 K and refined unit-cell parameters.

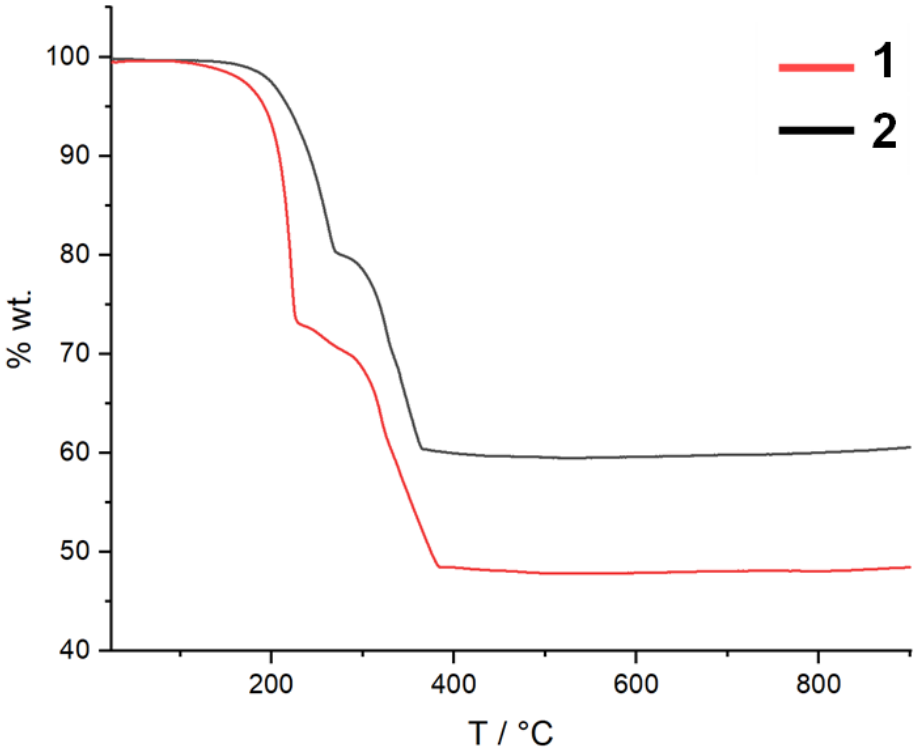

Figure S2. Thermograms of **1** and **2** show that both compounds present thermal stability in air until approximately 150°C. From this point, the total decomposition is approximately achieved around 400°C for both compounds.

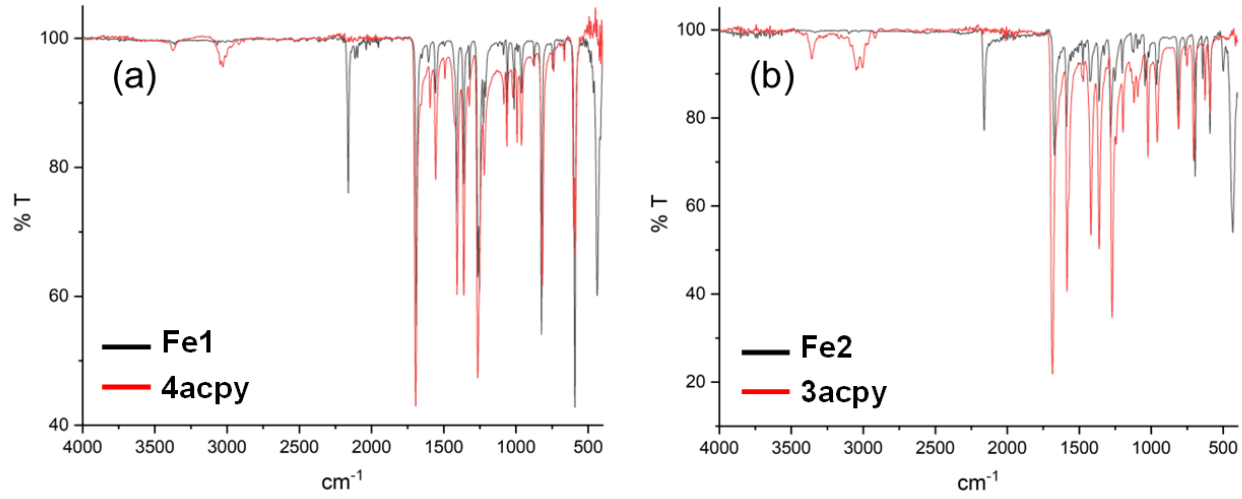

Figure S3. Infrared spectra of **1** (black) and 4-acetylpyridine (4acpy; red) and of **2** (black) and 3-acetylpyridine (3acpy; red). Compounds **1** and **2** present an IR pattern very similar to the one of the free ligands with characteristic $\overline{\nu}$(C=O) vibration of the ketone (1689 and 1671 cm^{-1} for **1** and **2** respectively). The characteristic $\overline{\nu}$(C≡N) is found at 2160 cm^{-1} in both cases belonging to $[Ag(CN)_2]^-$ fragment in the structure of **1** and **2**.

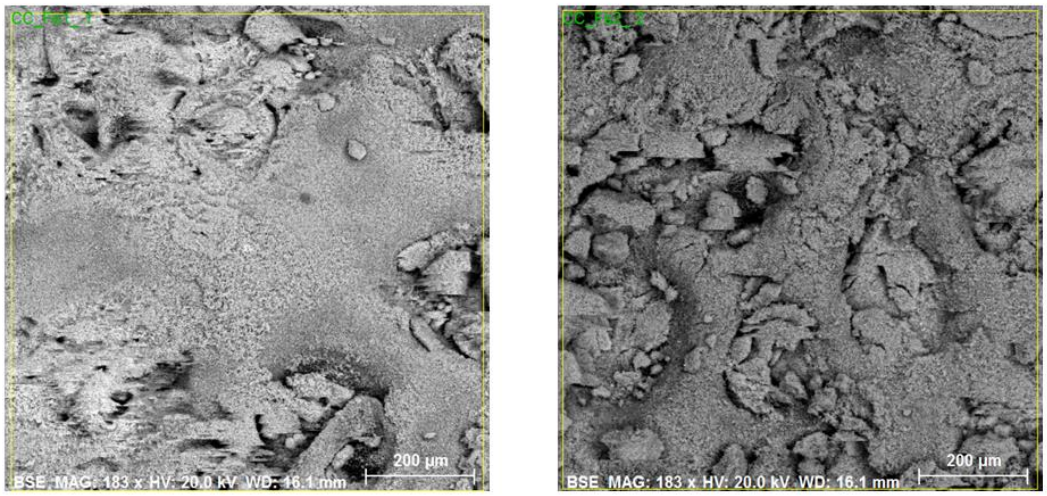

Fe-1	[wt.%]
Fe 26 K-series	19.11
Ag 47 L-series	39.87

Fe-2	[wt.%]
Fe 26 K-series	17.61
Ag 47 L-series	38.19

Figure S4. EDXS analysis for **1** and **2** with the estimated wt. % of Fe and Ag: 19.11 wt.% and 39.87 wt.% for Fe and Ag, respectively for **1**; and 17.61 wt.% and 38.19 wt.% for Fe and Ag, respectively for **2**. In both cases, the 1:2 ratio of Fe:Ag is confirmed.

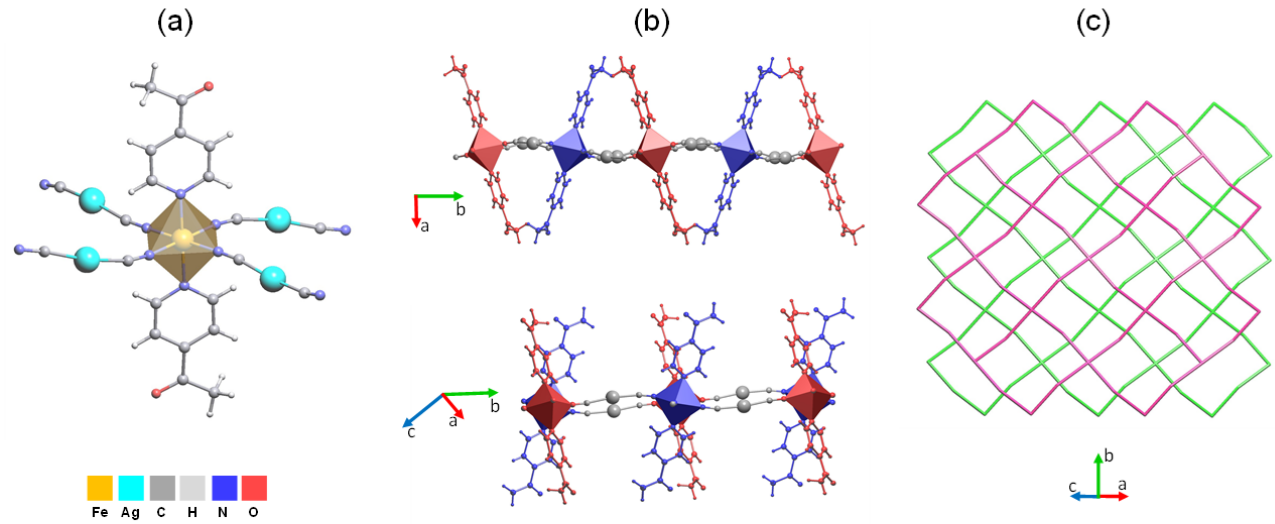

Figure S5. (a) View of the coordination environment of the Fe(II) site in **1** at 270 K. (b) View of the crystal structure highlighting the tilting of the 4acpy ligands above the 2D $\{Fe[Ag(CN)_2]_2\}$ coordination network in **1** at 270 K. (c) Schematic view of the stacking of the 2D $\{Fe[Ag(CN)_2]_2\}$ coordination networks in **1**.

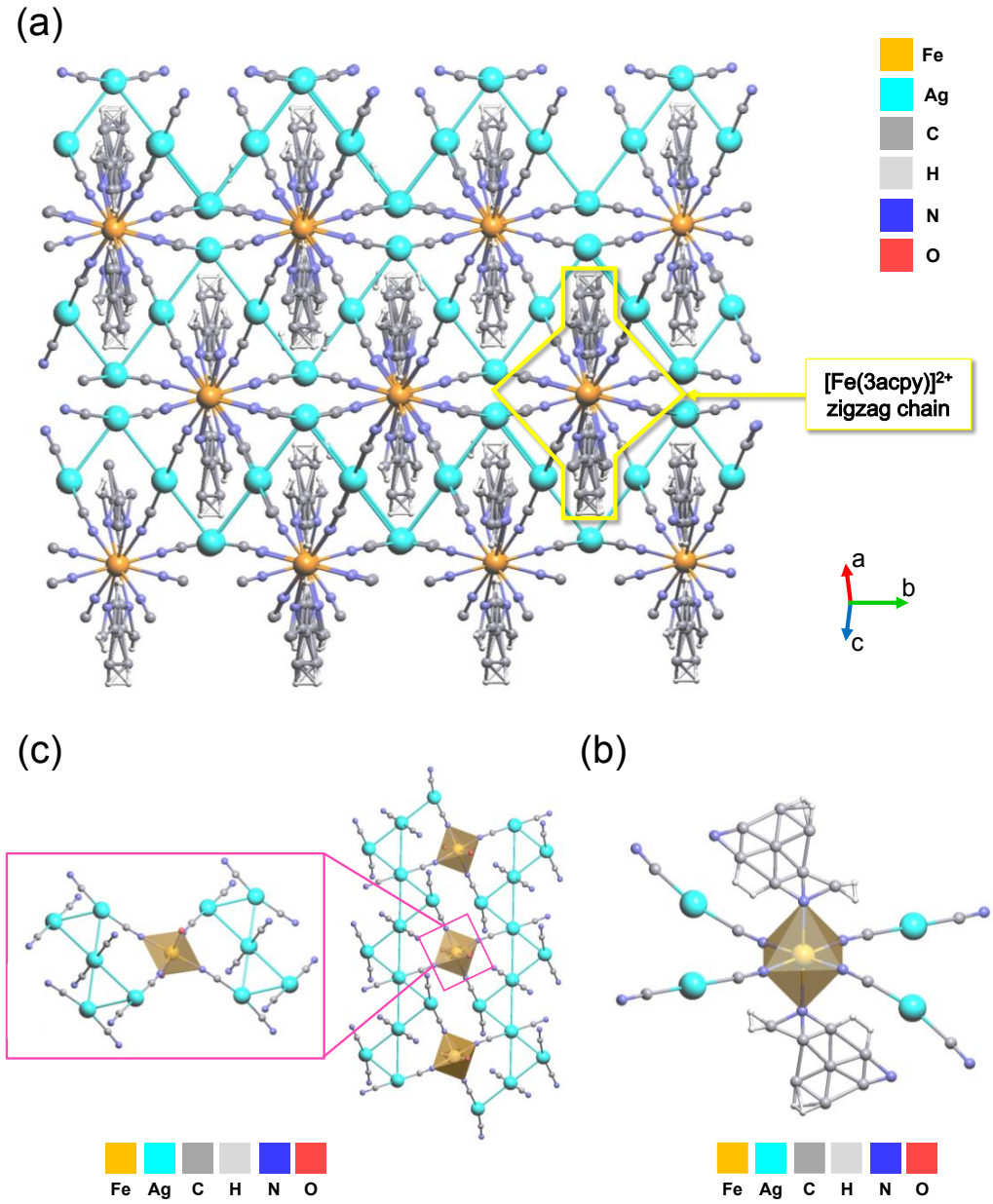

Figure S6. (a) View of $[Fe(3acpy)]^{2+}$ zigzag chain along the *a** axis at 296 K. (b) View of the $[Ag(CN)_2]_3^{3-}$ triangles that form a Ag-based chain running along the *c* axis at 96 K. Cyanido groups of this chain coordinate to the Fe(II) site in its four equatorial positions. (c) View of the coordination environment of the Fe(II) site in **2** at 296 K.

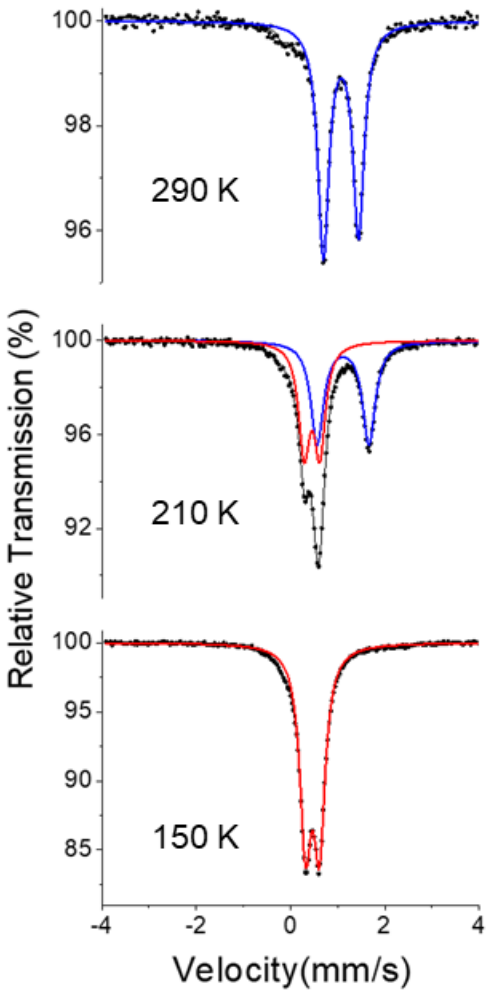

Figure S7. ^{57}Fe Mössbauer spectra for **1** at 150 K, 210 K and 290 K with the blue and red solid lines corresponding to the fit of the high-spin and low spin Fe centers, respectively. See Table 3 for the fitting parameters. In addition to the doublets corresponding to [FeN_6] site, there is a contribution to the spectrum area of less than 5% at about 0 mm s^{-1}. This contribution remains in all spectra at different temperatures. It may correspond to a small fraction of high-spin Fe(II) impurity.

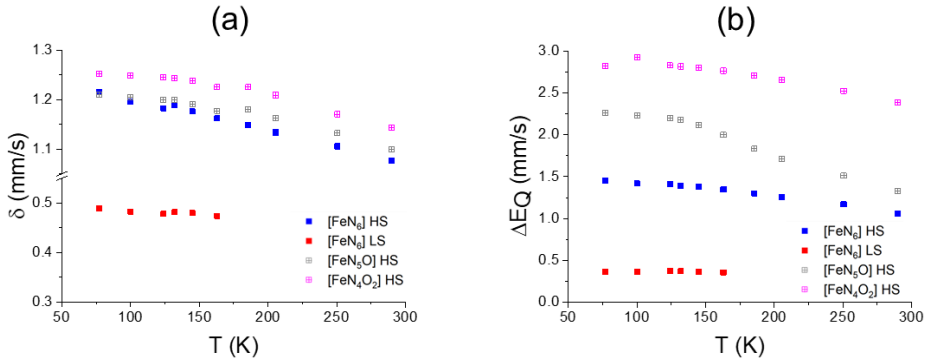

Figure S8. Thermal evolution of (a) the isomer shift (δ) and (b) quadrupole splitting (ΔE_Q) of the Mössbauer doublets for the different chemical environments of the Fe site in **2**.

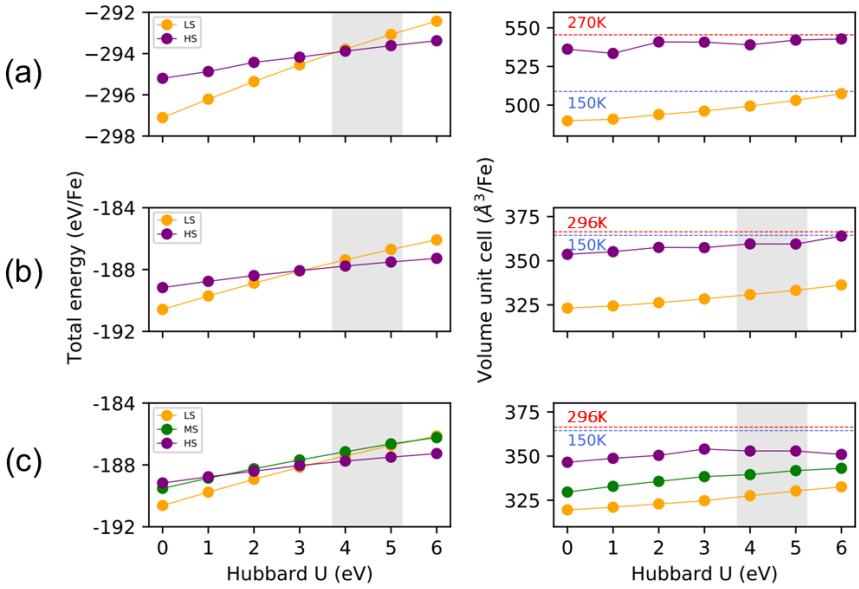

Figure S9. DFT+U total energies and unit cell volumes for (a) **1**, (b) **2** model 1, and (c) **2** model 2, as a function of Hubbard *U* parameter. Dash blue and red lines denote experimental values at 150 and 270 K, respectively. The highlighted gray area shows typical *U* values for Fe with an O environment. For **2**: *HS* = the four Fe sites with high spin; *LS* = the four Fe sites in low spin; *MS* = an intermediate case with an incomplete SCO in which two Fe sites with $[FeN_4O_2]$ remain in high spin and two $[FeN_6]$ sites are low spin.

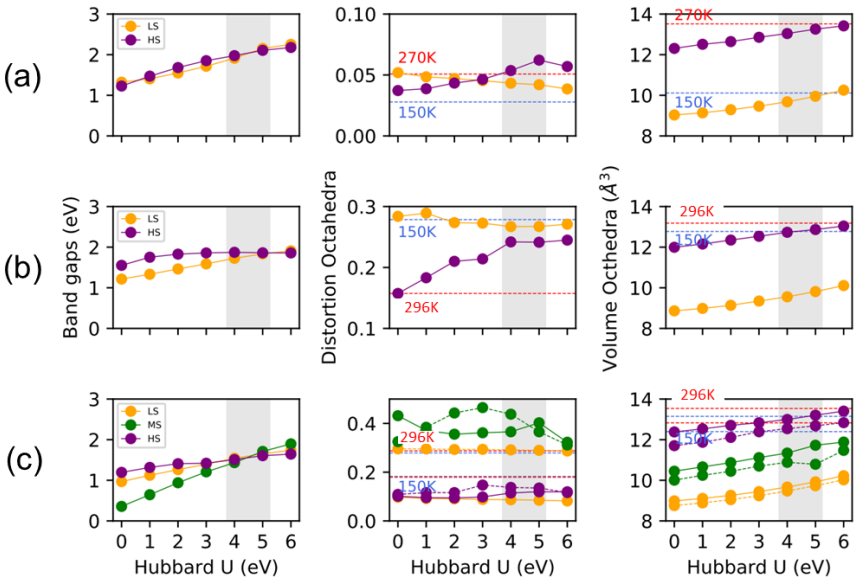

Figure S10. DFT+U band gaps (left), octahedral distortions (center), octahedral volumes (right) as a function of Hubbard *U* parameter for (a) **1**, (b) **2** model 1, and (c) **2** model 2. Dash lines denote experimental values at 150 K (blue line) and 270 K (red line) for **1** and 150 K (blue line) and 296 K (red line) for **2**. The highlighted gray area shows typical *U* values for Fe within an O environment. For **2**: *HS* = the four Fe sites with high spin; *LS* = the four Fe sites in low spin; *MS* = an intermediate case with an incomplete SCO in which two Fe sites with $[FeN_4O_2]$ remain in high spin and two $[FeN_6]$ sites are low spin.

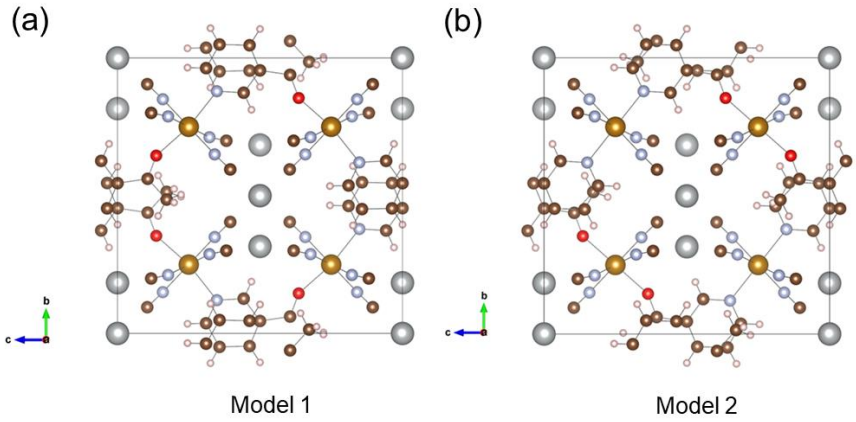

Figure S11. Schematic unit cell of the two theoretical models for **2**: (a) model 1 and (b) model 2.

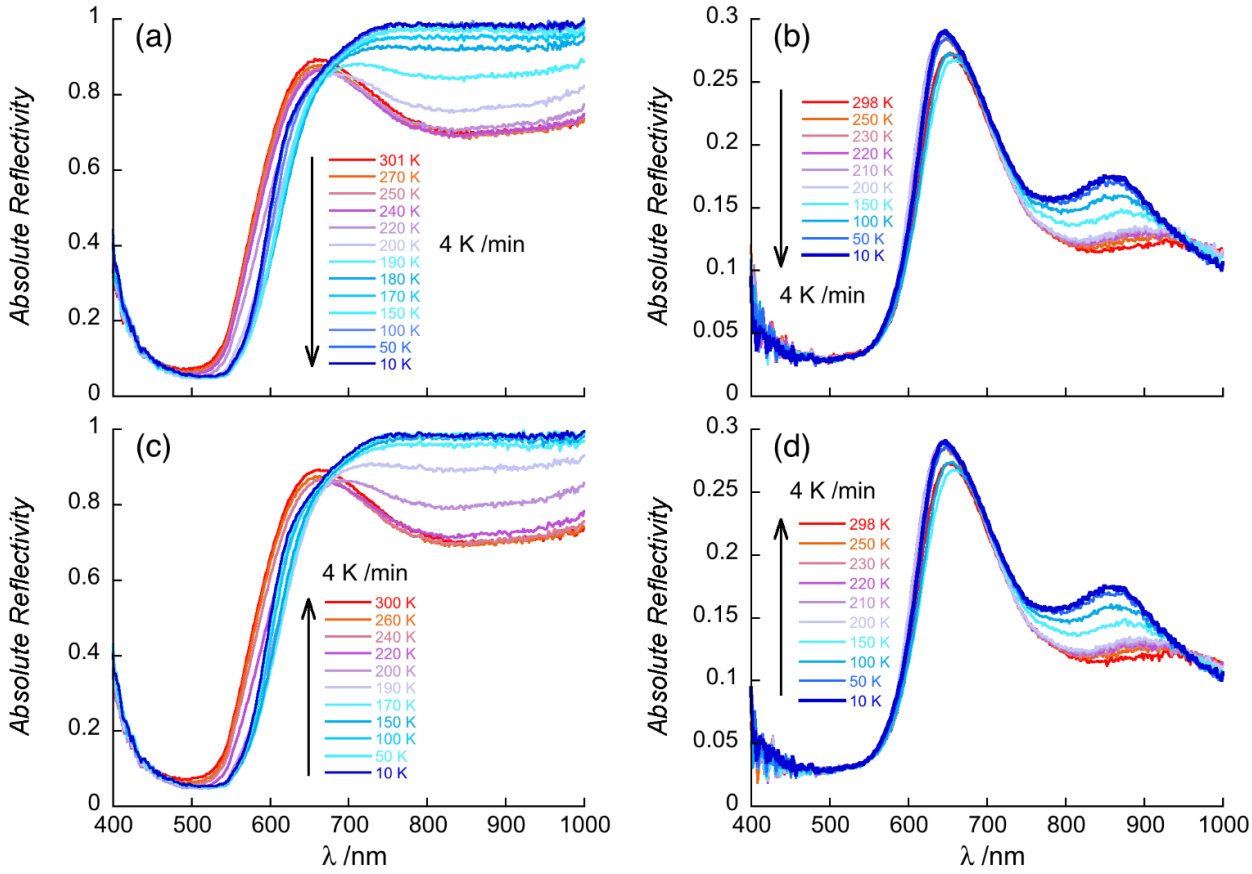

Figure S12. Optical reflectivity spectra between 400 and 1000 nm at selected temperatures decreasing the temperature from 300 to 10 K (a & b) and increasing the temperature from 10 K to room temperature (c & d) for **1** (a,c) and **2** (b,d). A spectroscopic white light of 0.08 mW cm^{-2} has been used for these measurements.

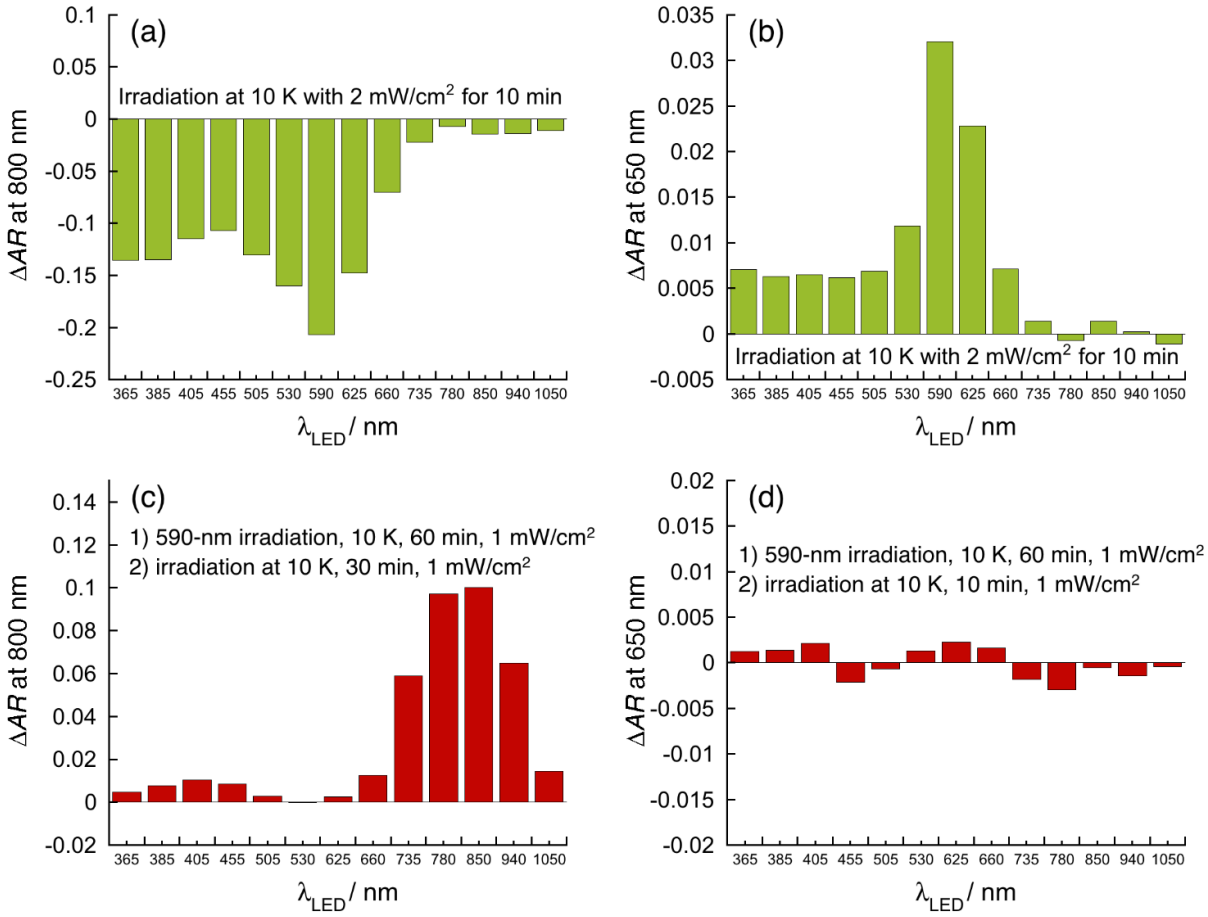

Figure S13. a & b: After a fast cooling of the sample from room temperature in the dark, the plots show the variation of the absolute optical reflectivity at 10 K comparing before and after excitation with different LEDs ($\Delta AR = AR_{after} - AR_{before}$; 10 minutes, at 2 mW cm^{-2}) for **1** (a; recorded at 800 nm) and **2** (b; recorded at 650 nm). Both compounds are photosensitive with LEDs of wavelengths below 625 nm with maximum efficiency obtained with the 590-nm LED. c & d: after a fast cooling of the sample from room temperature in the dark and a 590-nm irradiation of the sample at 10 K during 60 min (1 mW cm^{-2}), the plots show the variation of the absolute optical reflectivity at 10 K for **1** (c; recorded at 800 nm) and **2** (d; recorded at 650 nm) before and after desexcitation with different LEDs ($\Delta AR = AR_{after} - AR_{before}$; at 1 mW cm^{-2}). A spectroscopic white light of 0.08 mW cm^{-2} has been used for these measurements.

Supplementary Tables

Table S1. CShM calculation for Fe(II) environment in **1**-270 K
Table S2. CShM calculation for Fe(II) environment in **1**-150 K
Table S3. Total energies for **1** and **2**, obtained with DFT+U

Table S1. CShM calculation for Fe(II) environment in 1-270 K

```
-------------------------------------------------------------------------------
Ideal structures   ML6
HP-6          1 D6h   Hexagon
PPY-6         2 C5v   Pentagonal pyramid
OC-6          3 Oh    Octahedron
TPR-6         4 D3h   Trigonal prism
JPPY-6        5 C5v   Johnson pentagonal pyramid J2
-------------------------------------------------------------------------------
Structure     1    [Kostakis]
   Fe       0.0000   0.0000   0.0000
   N        0.8174  -1.2097  -1.5463
   N       -1.5486   0.7892  -1.3859
   N        1.2957   1.6294  -0.5209
   N       -1.2957  -1.6294   0.5209
   N        1.5486  -0.7892   1.3859
   N       -0.8174   1.2097   1.5463

 HP-6        Ideal structure    CShM =   32.47241
   Fe     M        0.0000   0.0000   0.0000
   N      L1       0.6168  -1.6205  -0.4004
   N      L3      -1.7229   0.3792  -0.2343
   N      L5       1.1060   1.2413   0.6347
   N      L2      -1.1060  -1.2413  -0.6347
   N      L6       1.7229  -0.3792   0.2343
   N      L4      -0.6168   1.6205   0.4004

 PPY-6       Ideal structure    CShM =   29.75396
   Fe     M       -0.0902   0.0631   0.2382
   N      L1       0.5415  -0.3784  -1.4293
   N      L2      -1.8051   0.0949  -0.4199
   N      L4       1.4070   1.0853   0.5348
   N      L6      -0.7981  -1.6228   0.4164
   N      L5       1.1871  -1.0107   1.0064
   N      L3      -0.4423   1.7686  -0.3467

 OC-6        Ideal structure    CShM =    0.05042
   Fe     M        0.0000   0.0000   0.0000
   N      L1       0.8351  -1.2062  -1.5922
   N      L2      -1.5017   0.7588  -1.3625
   N      L3       1.3171   1.6300  -0.5439
```

```
  N      L5       -1.3171  -1.6300   0.5439
  N      L4        1.5017  -0.7588   1.3625
  N      L6       -0.8351   1.2062   1.5922

TPR-6       Ideal structure    CShM =   16.51120
  Fe     M         0.0000   0.0000   0.0000
  N      L1        0.0297  -1.4629  -1.3322
  N      L4       -0.6791   1.0192  -1.5542
  N      L5        1.0218   1.6698   0.2886
  N      L3       -0.6971  -1.4480   1.1546
  N      L2        1.7306  -0.8122   0.5107
  N      L6       -1.4059   1.0341   0.9325

JPPY-6      Ideal structure    CShM =   33.10594
  Fe     M         0.0554  -0.0309  -0.1534
  N      L1        0.4520  -1.7990   0.3465
  N      L3       -1.2806   1.0860  -0.8612
  N      L4        0.7496   1.7129  -0.2544
  N      L2       -1.4645  -1.0845  -0.4898
  N      L5        1.8204  -0.0701   0.4920
  N      L6       -0.3323   0.1856   0.9201
-------------------------------------------------------------------------------
```

Table S2. CShM calculation for Fe(II) environment in 1-150 K

```
-------------------------------------------------------------------------------
Ideal structures   ML6
HP-6          1 D6h   Hexagon
PPY-6         2 C5v   Pentagonal pyramid
OC-6          3 Oh    Octahedron
TPR-6         4 D3h   Trigonal prism
JPPY-6        5 C5v   Johnson pentagonal pyramid J2
-------------------------------------------------------------------------------

Structure     1    [Kostakis]
  Fe       0.0000   0.0000   0.0000
  N        0.9316   0.0764  -1.7766
  N       -1.7051   0.3706  -0.8656
  N       -0.2766  -1.9075  -0.2144
  N        0.2766   1.9075   0.2144
  N        1.7051  -0.3706   0.8656
  N       -0.9317  -0.0764   1.7766

HP-6        Ideal structure    CShM =   32.79348
  Fe     M         0.0000   0.0000   0.0000
  N      L1        1.2699   0.5601  -0.8179
  N      L3       -1.3540   0.8693   0.0797
  N      L5        0.0841  -1.4294   0.7382
```

N	L2	-0.0841	1.4294	-0.7382
N	L6	1.3540	-0.8693	-0.0797
N	L4	-1.2699	-0.5601	0.8179

PPY-6 Ideal structure CShM = 29.98796

Fe	M	0.0587	0.2046	0.1058
N	L2	1.4370	0.2898	-0.8230
N	L4	-1.5486	0.6311	0.1722
N	L1	-0.3521	-1.2279	-0.6350
N	L3	-0.3118	1.0324	-1.2896
N	L6	1.2810	-0.5706	0.9272
N	L5	-0.5642	-0.3596	1.5423

OC-6 Ideal structure CShM = 0.02783

Fe	M	0.0000	0.0000	0.0000
N	L1	0.9062	0.0703	-1.7420
N	L2	-1.7193	0.3614	-0.8798
N	L3	-0.2889	-1.9301	-0.2282
N	L5	0.2889	1.9301	0.2282
N	L4	1.7193	-0.3614	0.8798
N	L6	-0.9062	-0.0703	1.7420

TPR-6 Ideal structure CShM = 16.67143

Fe	M	0.0000	0.0000	0.0000
N	L1	0.1224	-0.0953	-1.7871
N	L2	-1.4608	0.9577	-0.4084
N	L4	0.4808	-1.7232	-0.1324
N	L3	0.8009	1.5794	-0.2866
N	L6	1.1592	-0.0485	1.3681
N	L5	-1.1025	-0.6701	1.2464

JPPY-6 Ideal structure CShM = 33.42042

Fe	M	0.0391	0.1248	0.0739
N	L1	1.4555	0.2354	-0.8629
N	L3	-1.5962	0.5881	0.1569
N	L6	-0.2347	-0.7491	-0.4432
N	L2	-0.3152	1.0533	-1.3075
N	L5	1.2687	-0.7353	0.8763
N	L4	-0.6173	-0.5173	1.5066

Table S3. Total energies for 1 and 2, obtained with DFT+U

Spin	**2*** Model 1		**2*** Model 2		**1**	
	Energy (meV)	Bond lengths (Å)	Energy (meV)	Bond lengths (Å)	Energy (meV)	Bond lengths (Å)
LS	817	1.99 N1 1.94 N2 1.93 N3,4,5 1.98 O	568	2.00 N1,2 1.93 N3,4 1.93 N5,6 1.96 O1,2 1.95 N1,2 1.94 N3,4	270	2.01 N1,2 1.93 N3,4 1.92 N5.6
MS			425	2.16 N1,2 2.11 N3,4 2.09 N5,6 2.08 O1,2 2.00 N1,2 1.96 N3,4		
HS	0	2.21 N1 2.13 N2 2.11 N3,4,5 2.13 O	0	2.28 N1,2 2.15 N3,4 2.13 N5,6 2.17 O1,2 2.15 N1,2 2.13 N3,4	0	2.20 N1,2 2.13 N3,4 2.12 N5.6

Compound **2 is simulated by two separated Model: 1 and Model 2. For each structure, LS, HS and MS spin configurations are considered, as described in the main text.*